JEOL news
Volume 39 number 2, 2004
ISSN 0385-4426

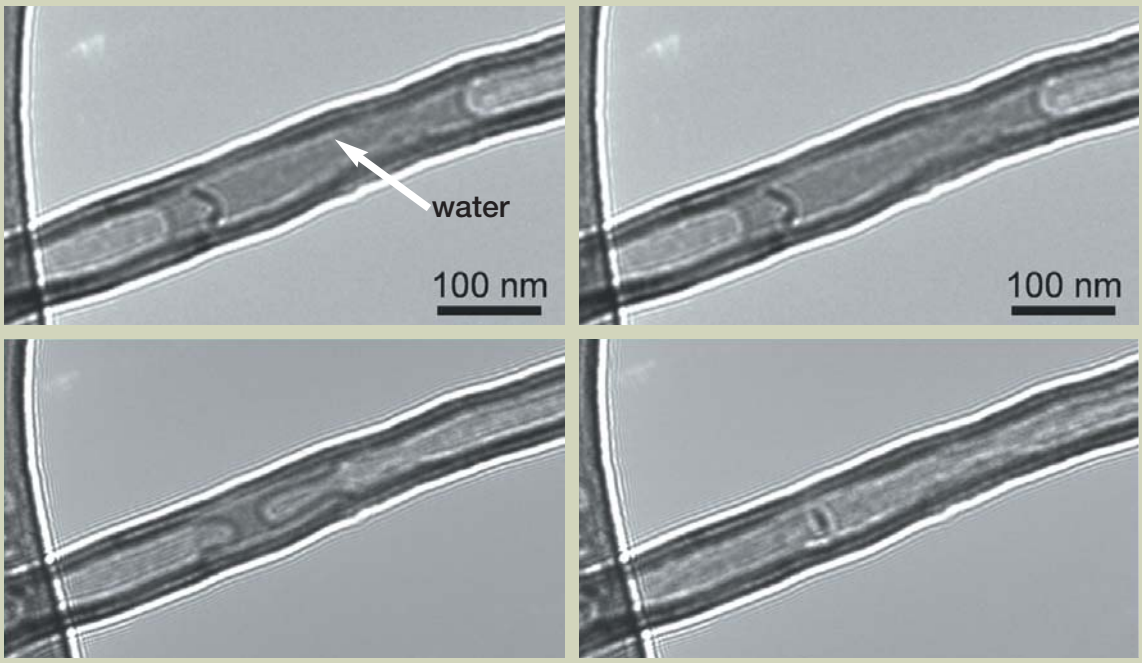

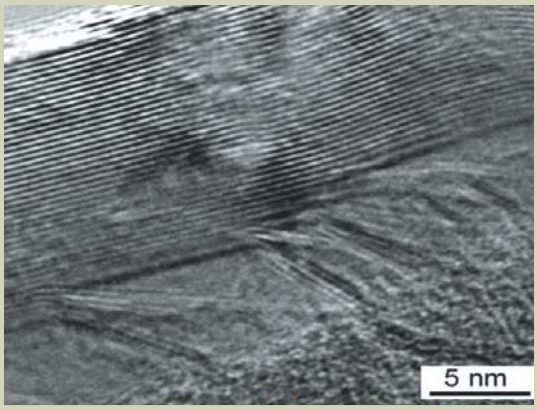

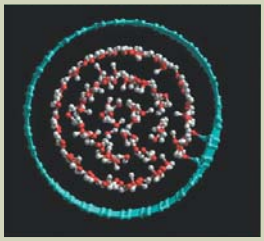

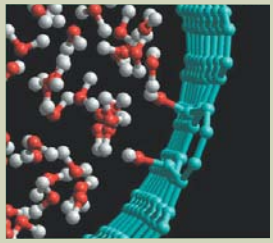

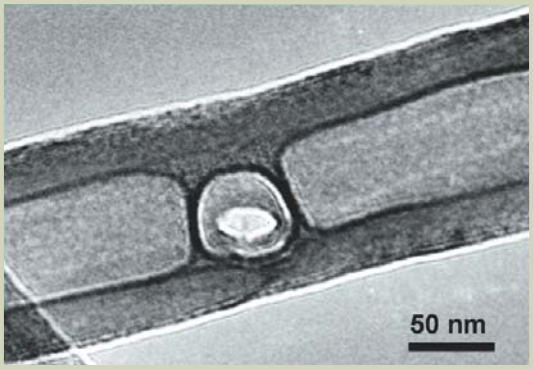

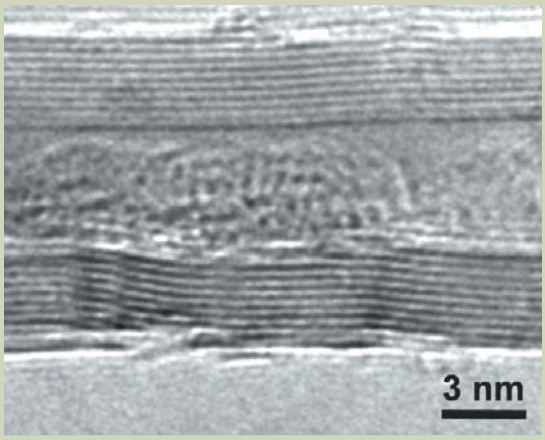

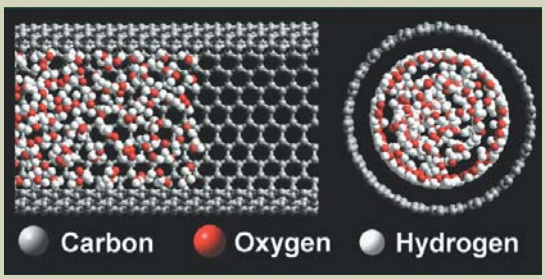

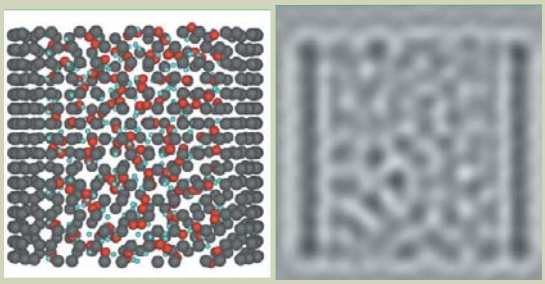

JEOL news

Volume 39 Number 2
November 30, 2004

TEM Study of Water in Carbon Nanotubes

Haihui Ye[1], Nevin Naguib, and Yury Gogotsi[2]

Department of Materials Science and Engineering and A. J. Drexel Nanotechnology Institute, Drexel University

High resolution transmission electron microscopy (HRTEM) and electron energy loss spectroscopy (EELS), supported by TEM simulation, show the presence of water in carbon nanotubes (CNT) subjected to hydrothermal treatment. It was observed that water behaves differently in the channels of CNT with different inner diameters. In large CNT (50 - 200 nm in diameter) water behaves fairly conventionally, showing a well-defined meniscus. Rapid evaporation and condensation upon the intensity change of electron beam, as well as strong interaction between nanotube walls and water, have been observed. Water in small CNT with inner diameter of 2 - 5 nm shows a surprisingly high contrast in HRTEM images. Fluidity of water in such small channels is greatly retarded compared to the macroscale. Both beam heating and electron bombardment in TEM play important role and affect water behavior in the small CNT. The present findings pose new challenges for modeling and device development.

Introduction

The properties of water in confinement differ from those of bulk water [1-3]. Fundamental understanding of water confined in nanometer-scale space is of great interest in biology, geology and materials science. Traditionally water is confined to a film between adjoining hydrophobic or hydrophilic surfaces to create a situation of confinement for experimental characterization [4, 5]. Use of CNT [6] provides a unique opportunity to investigate the water behavior in one-dimensional channels at nanometer scale, due to three reasons. First, various diameters of inner space of CNT are available, ranging from 0.4 nm [7] to hundreds of nanometers, which makes possible the studies of water behavior at different scales of confinement. Second, thin tube walls of CNT are transparent to X-rays, neutrons, electrons and even visible light, enabling the characterization of confined water by X-ray diffraction (XRD) [8], neutron scattering techniques [9], environmental scanning electron microscopy [10], optical microscopy [11], and TEM [12-15]. Third, the tube walls of CNT can be highly crystallized or disordered, forming a hydrophobic or hydrophilic inner surface respectively, which makes CNT an excellent container to study the interaction between water and the surroundings. On the other hand, the fact that CNT can be filled with water and used to transport water is of great value for numerous applications such as nanofluidic chips, cellular probes and capsules for drug delivery. Therefore, water behavior in confined systems, specifically in carbon nanotubes, is currently the subject of intense scrutiny [1-3, 8-15].

Recently, we demonstrated that autoclave treatment [12, 13] can be used to confine water in multi-walled nanotubes (MWNT) with inner diameters ranging from 100 nm to 2 nm. HRTEM and EELS investigations of the water behavior in these tubes will be described in this paper.

3141 Chestnut Street, Philadelphia, PA 19104, USA
[1]E-mail: haihui@drexel.edu
[2]E-mail: gogotsi@drexel.edu

Experiments and Characterization

Materials

Hydrothermal autoclave synthesis was used to produce large-diameter MWNT with water trapped inside as described in [12-14] from a mixture of ethylene glycol (Mallinckrodt, AR), distilled water and Ni powder (Aldrich, 100 mesh, 99.99%). Samples were produced at the University of Illinois at Chicago. The powder-

Contents

Cover micrograph

TEM micrographs of water in multi-walled carbon nanotubes and their simulated structures. The internal structures of the nanotubes and the interaction between the tube walls and water are clearly visible, together with molecular-mechanics simulated structures. (See pages 2 to 7.)

Courtesy of Dr. Haihui Ye, Department of Materials Science and Engineering and A. J. Drexel Nanotechnology Institute, Drexel University

JEOL
Serving Advanced Technology

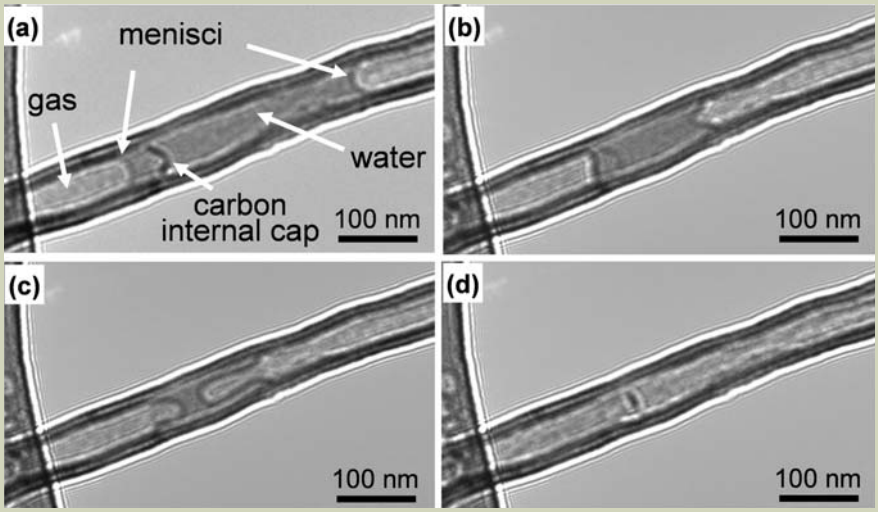

Fig. 1 TEM images of MWNT produced by hydrothermal treatment and containing a water plug. Upon electron beam heating, the plug shrank due to water evaporation from (a) to (c) and completely disappeared in (d). The position of water, gas, as well as menisci of water is indicated in (a). A carbon internal cap is also indicated, which is commonly present in MWNT. Apparently the internal cap leaks and does not block the motion of water.

like synthesis products were dispersed in alcohol and then a drop of the solution was placed on a carbon-coated copper grid for TEM observation.

Purified CVD-grown MWNT [16] with inner diameter of 2 - 5 nm were selected for filling experiments. The number of graphene layers in the walls of CVD-MWNT varied typically from 3 to 10. These MWNT are comparable in diameter to single wall carbon nanotubes (SWNT), for which most of the modeling work has been done to date. MWNT present an advantage over SWNT for in-situ TEM experiments, as they are more stable under the electron beam and their larger wall thickness decreases the probability of water loss during TEM study. Distilled water (H_2O) was used to fill the different types of nanotubes as described in ref [15]. The high temperature autoclave treatment was conducted under conditions similar to the ones used in above hydrothermal synthesis of MWNT but at lower temperatures. The MWNT were sealed with water in a gold capsule. The capsule was then treated in the autoclave at 300 - 650°C under 20 - 80 MPa pressure [15]. As a result, the MWNT were filled with water and ready for TEM observation.

Characterization

A JEOL JEM-2010F TEM with FasTEM control system, operated at 100 kV, with a point-to-point resolution of 0.23 nm (at 200 kV), was used for TEM analysis of water in MWNT. EDS analysis was conducted along with TEM studies. A Gatan parallel EELS spectrometer was used to confirm the presence of water inside the nanotubes. The energy dispersion was set to 0.1 eV/channel (for **Fig. 4a**) and 0.5 eV/channel (for **Fig. 4b**), respectively. All EELS analyses were conducted in the scanning transmission (STEM) mode of the JEOL JEM-2010F microscope. The STEM probe size was set to 1 nm. For EELS analysis on ice, cryo-TEM was conducted using liquid nitrogen as cooling medium. However, high

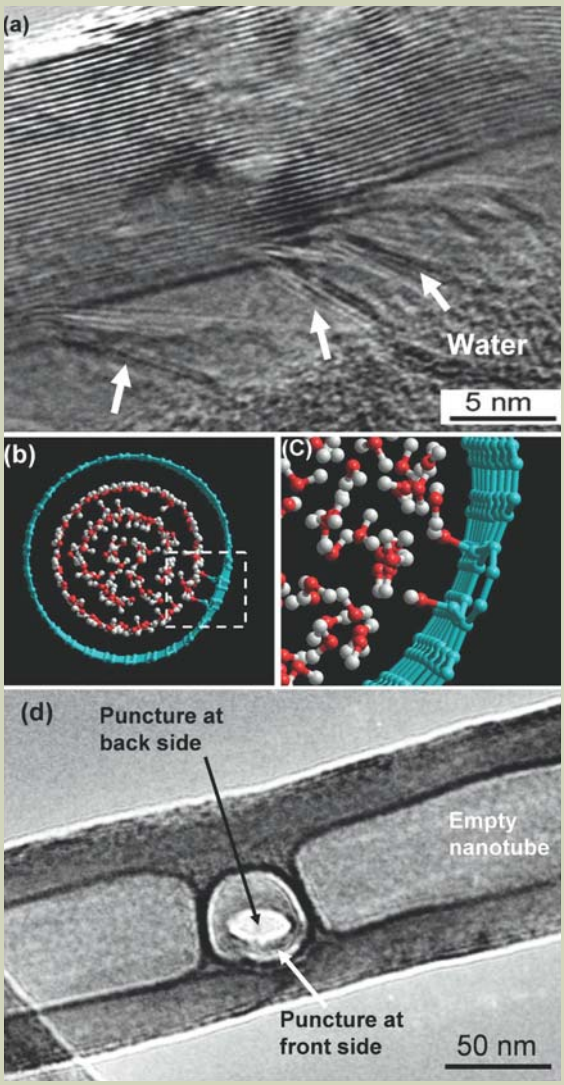

Fig. 2 TEM images showing the interaction between carbon tube walls and water. (a) Some graphene layers are peeled off from tube wall due to the strong water/carbon interaction [14]. (b) A HyperChem molecular-mechanics simulation shows that OH groups bonded to carbon atoms of CNT may drag the carbon atoms into water. (c) Enlarged image of (b). (d) Extreme heating with the electron beam causes the punctures of nanotube with formation of a through hole.

resolution TEM images of ice are not available because of image drift introduced by the evaporation of liquid nitrogen. Processing of TEM images and EELS spectra was accomplished using the Digital Micrograph program.

We accompanied TEM imaging with HyperChem modeling. HyperChem is a molecular modeling program. A Polak-Ribiere conjugate gradient algorithm was applied to optimize the molecular structure. HyperChem snapshots show water inside nanotubes of diameters equal to the tubes studied experimentally and observed under TEM in this work. Simulation was done for armchair SWNT that can be considered as inner shells of MWNT. The chirality of the latter is not known.

Multislice TEM simulation was performed using EMS program. The crystal information on carbon nanotube with water was acquired from HyperChem to build the first crystal for simulation. In EMS, a positive defocus means under focus. Different defocus settings with a certain defocus step were selected to obtain focal series images. The setup of the illumination and imaging system was the same as that of the JEOL microscope with an accelerating voltage of 100 kV and a coefficient of spherical aberration C_s of 1 mm.

Results and Discussion

Water in large nanotubes with diameter of 50 - 200 nm

TEM image of a typical MWNT produced hydrothermally is shown in **Fig. 1a**. This MWNT has an outer diameter of approximately 90 nm, wall thickness of 20 nm, and contains a liquid inclusion with a length of about 360 nm along the tube axis and volume of ~7 $\times$ 10^{-19} liter (0.7 attoliters). The fluid is mainly H_2O with a small amount of dissolved CO_2 and CH_4 according to thermodynamic calculations [17]. It is worth noting that water has a relatively low contrast compared with carbon nanotubes. This is understandable because water molecules do not scatter electrons as strongly as crystalline carbon sheets. To make the water in MWNT clearly visible, we greatly defocused the image and observed a special form of phase contrast termed Fresnel contrast. As a result, the meniscus of water-gas interface can be distinguished in **Fig. 1a**. The price we paid by using strong Fresnel contrast is the presence of sharp white lines at the outer surface of the carbon nanotube. Such contrast-increasing method is not necessary for high resolution TEM images of water, because electron diffraction and interference determine the contrast of high resolution TEM images. At certain observation conditions, water molecules can show much higher contrast than carbon atoms. It will be discussed in details in the next chapter.

During TEM observation, the fluid inclusion demonstrated volume contraction or expansion upon heating/cooling achieved by manipulating the illuminating electron beam, as reported in [13, 18]. **Fig. 1** shows a sequence of images demonstrating the fluid contraction upon electron beam heating until the fluid totally disappears. The process from **Fig. 1a** to **Fig. 1b** is reversible when the brightness of the electron beam is reduced. The fluid contraction may result from liquid evaporation within the tube or transport along the tube wall, while volume recovery could occur via condensation from the gas phase. It has been often disputed whether beam heating or radiolysis plays a more important role in energy transfer to water molecules. It is clear in our TEM observation that beam heating can readily raise the temperature of water from room temperature up to near its boiling temperature and cause rapid water evaporation. Considering that the inner vapor pressure of MWNT is much higher than atmospheric pressure due to autoclave treatment, we can speculate that the temperature has been raised to above 100°C to evaporate the water. Therefore electron beam heating plays a dominant role in this situation. Another evidence in favor of heating is that radiolysis is an irreversible process, which cannot explain the reversible contraction/ expansion of the liquid plug observed between **Fig. 1a** and **Fig. 1b**. Reversible water transport between the ends of a closed nanotube has been recently demonstrated by using even a higher accelerating voltage in TEM [19]. The demonstration that TEM can heat water above 100°C without the assistance of a heating stage might be helpful to understand the strong beam heating effect of TEM in other materials.

Fig. 1c shows that during the volume contraction, water meniscus changes its shape, demonstrating a strong interaction between the tube walls and water. Strong interaction between the enclosed water and the nanotube walls can be imaged by HRTEM with lattice resolution, as shown in **Fig. 2a**. The water trapped in the nanotube shown in **Fig. 2a** has undergone violent evaporation due to strong beam heating in TEM. Some graphene layers were found to be peeled off from the tube wall bending toward the tube axis. Such observation might be explained by the interaction between = O or –OH terminated graphite layers and water. Hydrogen bonding appears to be strong enough to overcome van der Waals interaction between graphite layers in the tube wall and pull the graphite layers away from the inner tube surface. A HyperChem molecular-mechanics simulation (**Figs. 2b** and **2c**) shows when carbon atoms in the tube wall of CNT are bonded to OH groups, the OH groups tend to drag the carbon atoms toward water, in agreement with the experimental observation in **Fig. 2a**. When the electron beam in TEM is converged rapidly and precisely on the region of the water inclusion, a puncture of the nanotube can be instantly observed, as shown in **Fig. 2d**. This is an extreme situation of water-MWNT interaction. We have tried to converge the electron beam on empty MWNT and only ended up with gradual deformation of the whole nanotube, a typical situation described in Ref. [20]. Therefore the presence of water is critical for puncture. Because water is not a good heat conductor, it can be heated to a very high temperature, which enables the strong water-MWNT interaction by reaction $2C + 2H_2O \rightarrow CH_4 + CO_2$. Water may rapidly penetrate between graphite layers and pull out the tube walls, by a process shown in **Fig. 2a**, consequently etching the tube walls until the puncture appears. This new method of using the electron beam in TEM to machine carbon nanotubes provides a way to drill holes in carbon nanotubes, which could be useful in some potential applications, for example, fabrication of nanofluidic devices.

Water in small nanotubes with diameter of 2 - 5 nm

The above results and discussion show the feasibility of filling MWNT with water and some important features of water-MWNT interaction. Slow water dynamics is observed at this scale of confinement (50 to 200 nm), but a conventionally shaped meniscus was observed in these MWNT, even in the 10-nm-diameter MWNT [15]. However, when MWNT with 2 - 5 nm in diameter (**Fig. 3a**) were filled with water, we discovered a different water behavior. After autoclave treatment, the MWNT were partially filled with water, as shown in **Fig.3b**. The contrast of the water inclusion in **Fig. 3b** is high.

To confirm that the material inside the tube was water and not amorphous carbon or hydrocarbons trapped during filling or synthesis, EELS analysis of the nanotubes, before and after filling, including spectral imaging in scanning transmission electron microscopy (STEM) mode were performed. Previous EELS work [21] conducted on crystalline ice demonstrated that the corresponding spectra have a characteristic peak in the low loss region (9.1 eV), which corresponds to water molecule excitation. When we filled nanotubes produced by chemical vapor deposition (CVD) with water and cooled them down to –80°C, an EELS peak at the same position was recorded (spectrum **I** in **Fig. 4a**), confirming the presence of ice. For comparison, EELS spectra of an empty nanotube (spectrum **II**) and a supporting carbon film (spectrum **III**) were also recorded. They did not show the characteristic peak of ice. The first high energy plasmon peak at 22.8 eV of MWNT with ice is consistent with that of the empty MWNT, as indicated by a dashed line. The second plasmon peak at 27.3 eV can be attributed to the supporting carbon film, as indicated by the second dashed line, because the investigated MWNT with ice was located on the carbon film. Because the sample was observed in the high vacuum (1.5 $\times$ 10^{-5} Pa) of the TEM for a prolonged time before cooling, no water adsorbed on the outer surface of the nanotubes could be sustained. Therefore, the peak at 9.1 eV in **Fig. 4a** may only originate from the ice entrapped inside the nanotube channels. The present peak at 9.1 eV is more blunt than the one reported in Ref. [21], probably due to the scattering effect of carbon surrounding the ice and confinement inside a nanometer channel. A typical EELS spectrum acquired from nanotubes at room temperature is shown in **Fig. 4b**. The features at 284 and 532 eV correspond to carbon K-edge and oxygen K-edge, respectively. The π^* peak of carbon K-edge reveals the sp^2-type bonding in the graphitic tube walls of the MWNT. Because STEM has a precise electron-beam probe with a size of 1 nm in diameter, the oxygen edge detected from the center of a carefully selected nanotube can only be attributed to water inside or oxygen-containing functional groups attached to the nanotube walls, not catalyst particles at the tip of the MWNT. Combining the EELS results in **Figs. 4a** and **4b**, it is inferred that the investigated nanotubes have water entrapped in their chan-

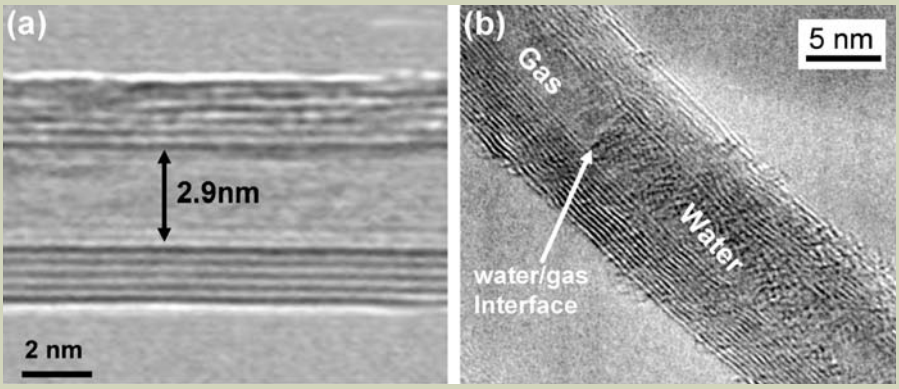

Fig. 3 (a) TEM image showing an empty CVD nanotube with inner diameter of 2.9 nm. (b) After autoclave treatment, water is observed in the nanotube channels. But it does not show a meniscus at the water/gas interface.

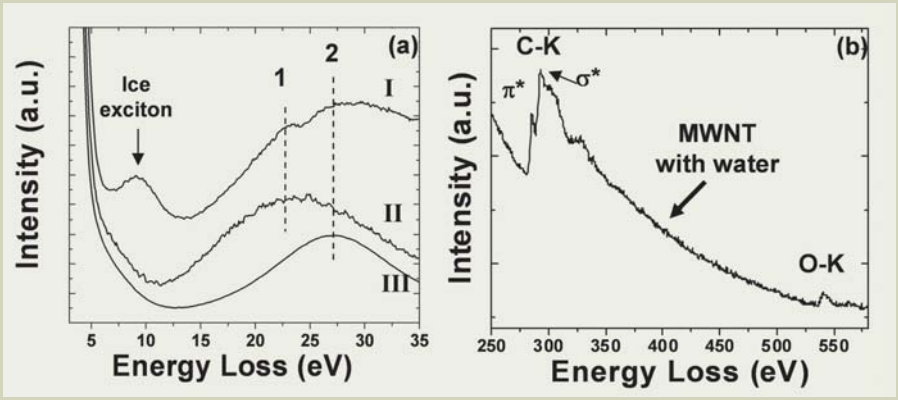

Fig. 4 (a) EELS spectra of a MWNT with ice at –80°C lying on the supporting carbon film (spectrum **I**), of an empty MWNT (spectrum **II**) and of the supporting carbon film (spectrum **III**). The peak at 9.1 eV corresponds to ice exciton. The plasma peaks are marked by the numbers 1 and 2 and are discussed in the text. (b) EELS spectrum of a MWNT with water at room temperature, showing C K-edge and O K-edge. σ* and π* peaks are noted for graphitic carbon [15].

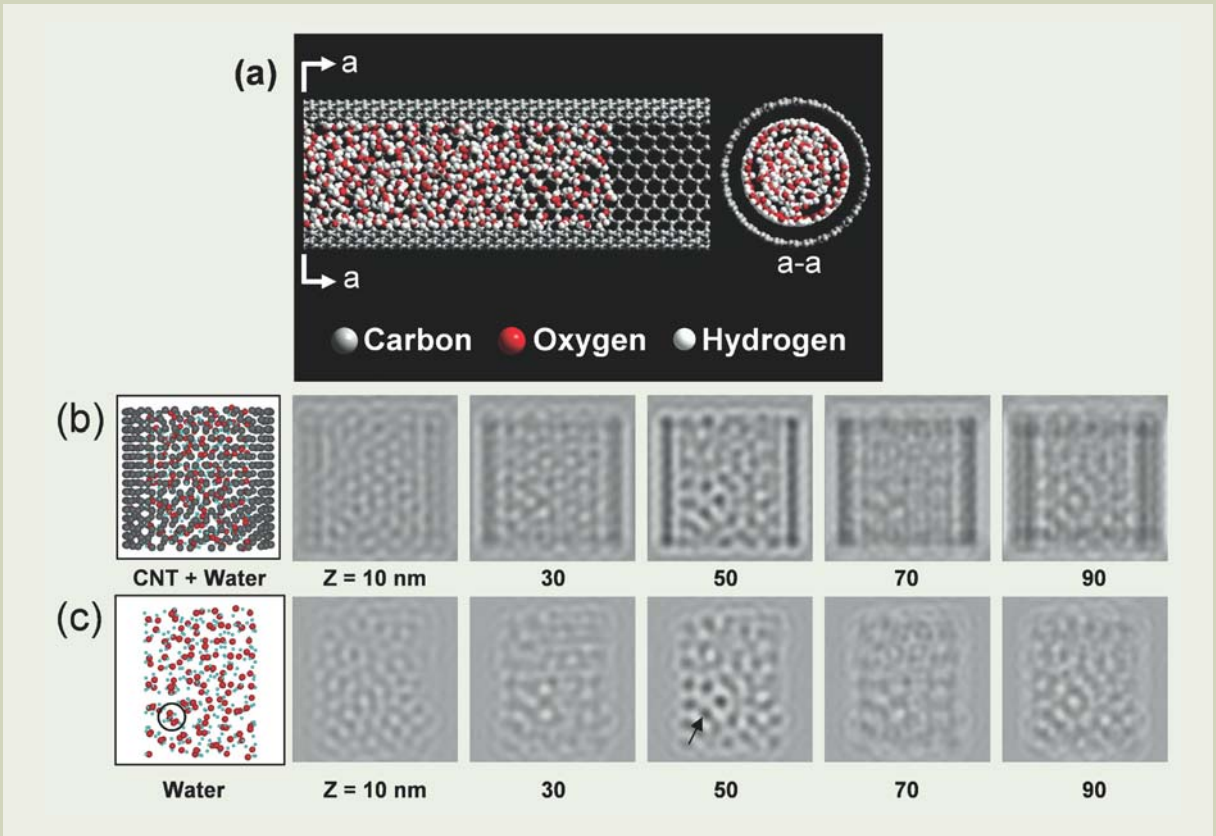

Fig. 5 (a) HyperChem simulation of water in a (30, 30) nanotube of 4.07 nm diameter, illustrating how water is arranged inside the nanotube of the same diameter as in Fig. 3b. Cross sectional snapshot (a - a) on the right indicates a high-density layer near the wall, but no interaction between water and the nanotube wall. (b, c) Simulated TEM images with different defocus values Z. The positive value means under focus. The images in (b) are generated from a (30, 30) nanotube containing water molecules. The images in (c) are from water molecules only. The model structures produced by HyperChem are shown on the left side. The simulated image of the nanotube with water at a defocus Z value of 50 nm matches our experimental image Fig. 3b. The black dots in simulated images of water (c) correspond to a cluster of water molecules, as indicated by an arrow and a circle [15].

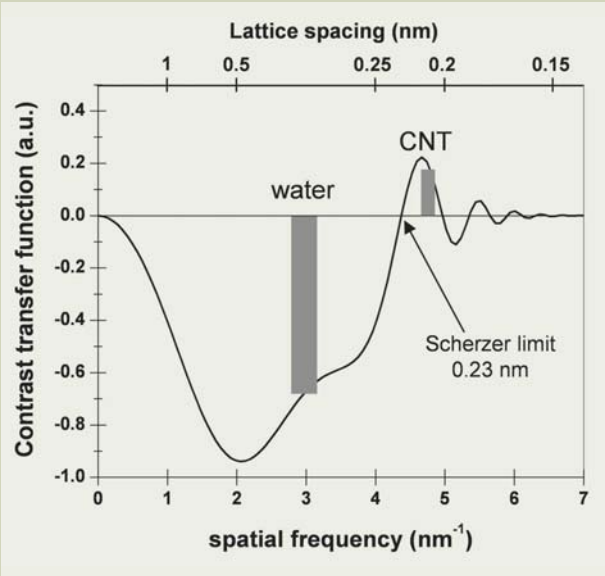

Fig. 6 A chart of contrast transfer function versus spatial frequency under Scherzer defocus condition of the TEM. The gray bars indicate the spacing for water and CNT, which can be used to explain the relatively high contrast of water in HRTEM.

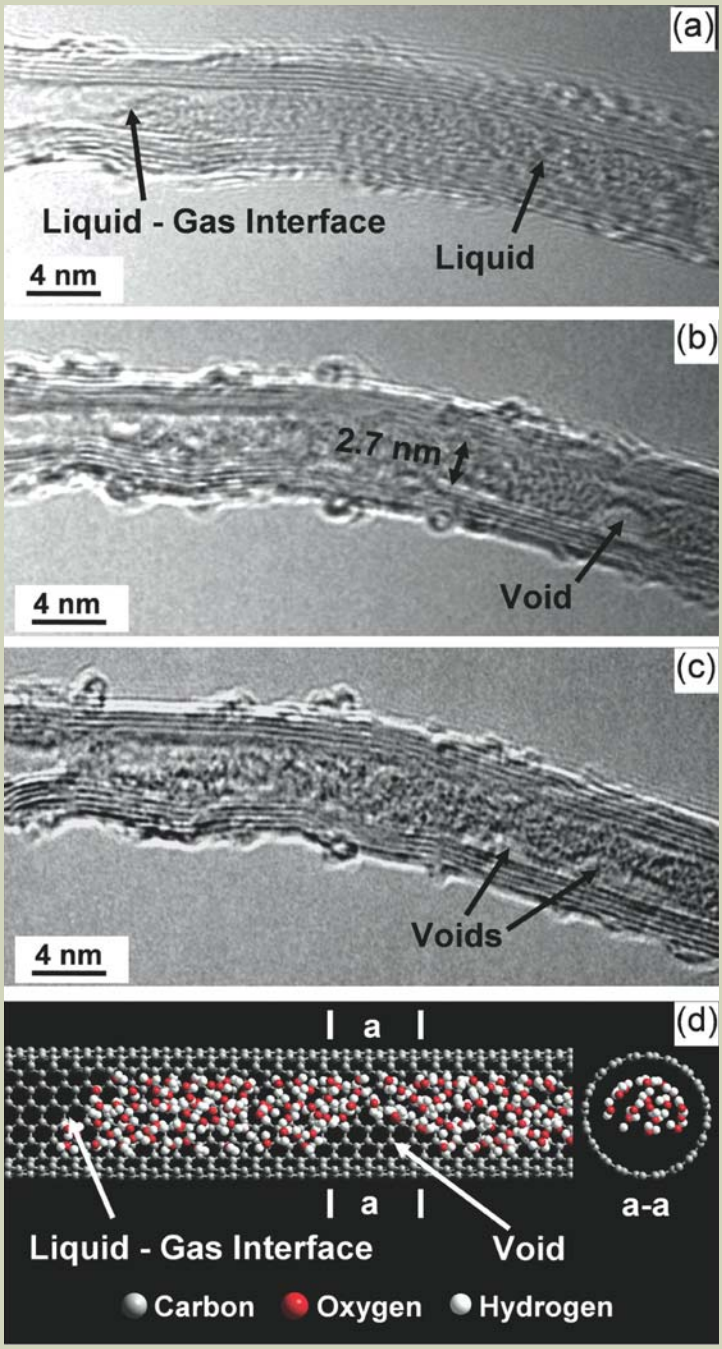

Fig. 7 Dynamics of water in a small MWNT. (a) A nanotube partially filled by water. (b) A nanosized bubble appears as the electron beam of TEM is focused on the nanotube. (c) After nearly one minute, two nanobubbles appear. The arrows indicate the position of nanobubbles. The motion of water is slow at this scale of confinement. (d) HyperChem simulation of this process [15].

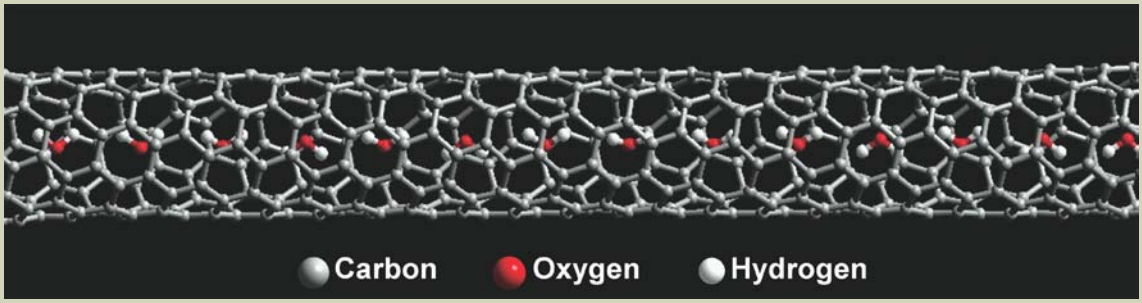

Fig. 8 HyperChem simulation of a SWNT ((6, 3) nanotube, diameter = 0.62 nm) filled by water. Simulation shows that water molecules are expected to from a chain inside the tube.

nels.

It has been demonstrated that defocusing has to be applied to discern the water in MWNT at low TEM magnification (**Fig. 1**). The surprisingly high contrast of water achieved in high resolution TEM can be understood by analyzing the results of TEM simulation. A crystal model of water in a carbon nanotube (**Fig. 5a**) was first built using HyperChem program. The structural HyperChem simulation conducted for water in a (30, 30) carbon nanotube of 4.07 nm diameter shows a random distribution of water molecules in the nanotube channel, which is in agreement with that observed in **Figs. 3b** and **3c**. Based on the HyperChem model, **Figs. 5b** and **5c** show the multislice TEM simulations produced for water molecules inside a (30, 30) carbon nanotube and water molecules without any nanotube surrounding them, respectively. The focal series of images correspond to different defocus Z from 10 to 90 nm, with an increment $\Delta Z = 20$ nm. This simulation shows that the water molecules are able to produce a strong contrast in the high resolution TEM images when the focal conditions are appropriate, in spite of their small molecular size and random distribution. Optimum adaptation of simulated images (**Fig. 5b**) to the experimental TEM image (**Fig. 3b**) is achieved for a defocus setting of 50 nm. It is worth noting that the black dots in the simulated TEM image for water, such as that indicated by an arrow in **Fig. 5c**, correspond to a cluster of adjoining water molecules (as indicated by a circle in the model structure of **Fig. 5c**, containing 4 molecules), rather than a single water molecule. Better TEM imaging conditions are required to resolve single molecules in a cluster.

Comparing the simulated images for defocus setting of 50 nm in **Fig. 5b** and **Fig. 5c**, we can clearly see black dots corresponding to clusters of water molecules, while no detail of carbon network is visible inside the nanotube. To understand this simulation results, we draw and analyze a chart of the contrast transfer function (CTF) versus spatial frequency under the Scherzer defocus condition (optimum defocus condition), as seen in **Fig. 6**. The average spacing of water clusters is about 0.3 -0.4 nm, as measured in HyperChem program, which is indicated by the gray bar for water in **Fig. 6**. The corresponding transfer function is about -0.7, which means the information of water is highly transmitted and the molecules appear dark. In contrast, the carbon network has an inter-chain spacing of 0.213 nm [22], smaller than the Scherzer limit (0.23 nm) of our TEM, as indicated by the gray bar for CNT in **Fig. 6**. Therefore the transfer function is only about 0.2, resulting in a poor contrast and the carbon atoms appearing bright. As a consequence, black dots of water clusters against a bright and vague background of carbon network is what we should be able to see at the optimum defocus condition, in agreement with the experimental observations (**Fig. 3b**).

Studies on large-diameter MWNT (**Fig. 1**) have shown a strong beam heating effect. When water in a 4-nm-MWNT (**Fig. 7a**) is exposed to electron beam, nanobubbles start to form with one bubble present in **Fig. 7b** and then two bubbles in **Fig. 7c**. A HyperChem simulation is drawn to illustrate the formation of nanobubbles in CNT, as shown in **Fig. 7d**. This could be attributed to evaporation of the liquid, similar to what happened in large MWNT. However, the effect of beam bombardment cannot be neglected at this confinement scale, because the formation of nanobubbles appears irreversible. It is plausible that both beam heating and electron bombardment contribute to the formation of nanobubbles. The time interval between the events shown in **Fig. 7b** and **Fig. 7c** is nearly one minute. Given the fine length scales L of these water volumes (L~10 - 100nm), and considering typical values of self-diffusion of bulk liquid water at atmospheric pressure (D~10^{-9} m^2/s), one would expect such processes to occur over characteristic times of L^2/D, or several microseconds. To this end, the characteristic times for the phenomena observed in **Fig. 7** are several orders of magnitude longer than expected, as based on macroscopic transport properties of water. This contradicts the prediction that confined water retains its bulk fluidity [3]. Increased water viscosity in confined spaces [5] may be responsible for the observed behavior. The slow response of water could also be due to the local presence of hydroxyl groups [14] on the inner tube walls after hydrothermal treatment. Water molecules could be pinned to these hydroxyl groups forming strong hydrogen bonds, which may lead to the ice-like behavior. In addition, van der Waals forces between tube walls and water molecules may play an important role in decreasing the mobility of water.

Water in single wall carbon nanotubes

It is predicted that water molecules form chains in the SWNT, as shown in HyperChem simulation **Fig. 8**. This simulation is in agreement with other publications [2, 23]. We found it was very difficult to observe water when we performed autoclave treatment on SWNT. While we observed chain-like structures inside SWNT, we were not able to conduct micro-analysis on single molecular chains and confirm that the tubes were filled with water. There are many obstacles that need to be overcome to observe water in single wall nanotubes, such as the TEM conditions, autoclave-treatment procedures, and quality of raw SWNT. This work is still in progress.

Conclusion

CNT with inner diameter above 2 nm can be filled with water. Water in large CNT (50 - 200 nm) shows a clearly distinguishable meniscus and slow liquid motion, while water in small CNT with 2 - 5 nm in diameter shows extremely slow motion upon electron beam irradiation in TEM. Strong interaction between carbon tube walls and water can be stimulated by the electron beams. Water confined in small CNT can be observed by HRTEM with a relatively high contrast.

Acknowledgement

We thank Dr. M. Yoshimura, TIT, Japan, for his help with the autoclave filling experiments, Dr. A.G. Yazicioglu and Dr. C.M. Megaridis, UIC, for producing hydrothermal nanotubes and for helpful discussions, and Dr. D. Luzzi, University of Pennsylvania, for advice on TEM simulation. TEM and EELS were performed at Penn Regional Nanotechnology Facility, University of Pennsylvania. This work was supported by NSF-NIRT grant CTS-0210579.

References

[1] Levinger, N.: *Science*, **298**, 1722-1723 (2002)
[2] Hummer, G., Rasaiah, J. C. and Noworyta, J. P.: *Nature*, **414**, 188-190 (2001)
[3] Raviv, U., Laurat, P. and Klein, J.: *Nature*, **413**, 51-54 (2001)
[4] Zhang, X., Zhu, Y. and Granick, S.: *Science*, **295**, 663-666 (2002)
[5] Zhu, Y. and Granick, S.: *Phys. Rev. Lett.*, **87**, 0961041-0961044 (2001)
[6] Iijima, S.: *Nature*, **354**, 56-58 (1991)
[7] Qin, L.-C., Zhao, X., Hirahara, K., Miyamoto, Y., Ando, Y. and Iijima, S.: *Nature*, **408**, 50 (2000)
[8] Maniwa, Y., Kataura, H., Abe, M., Suzuki, S., Achiba, Y., Kira, H. and Matsuda, K.: *J. Phys. Soc. Jap.*, **71**, 2863-2866 (2002)
[9] Beta, I. A., Li, J. -C. and Funel, B.: *Chem. Phys.*, **292**, 229-234 (2003)
[10] Rossi, M. P., Ye, H., Gogotsi, Y., Babu, S., Ndungu, P. and Bradley, J. C.: *Nano Lett.*, **4**, 989-993 (2004)
[11] Kim, B. M., Sinha, S. and Bau, H.: *Nano Lett.*, **4**, 2203-2208 (2004)
[12] Gogotsi, Y., Libera, J. and Yoshimura, M.: *J. Mater. Res.*, **15**, 2591-2594 (2000)
[13] Megaridis, C. M., Guvenc-Yazicioglu, A., Libera, J. A. and Gogotsi, Y.: *Phys. Fluids*, **14**, L5-L8 (2002)
[14] Ye, H., Naguib, N., Gogotsi, Y., Yazicioglu, A. G. and Megaridis, C. M.: *Nanotechnology*, **15**, 232-236 (2004)
[15] Naguib, N., Ye, H., Gogotsi, Y., Yazicioglu, A. G., Megaridis, C. M. and Yoshimura, M.: *Nano Lett.*, **4**, 2237-2243 (2004)
[16] Su, M., Zheng, B. and Liu, J.: *Chem. Phys. Lett.*, **322**, 321-326 (2000)
[17] Libera, J. and Gogotsi, Y.: *Carbon*, **39**, 1307-1318 (2001)
[18] Gogotsi, Y., Libera, J., Guvenc-Yazicioglu, A. and Megaridis, C. M.: *Appl. Phys. Lett.*, **79**, 1021-1023 (2001)
[19] Yazicioglu, A. G., Megaridis, C. M. and Gogotsi, Y.: *ASME J. Heat Transfer*, **126**, 506 (2004)
[20] Smith, B. W. and Luzzi, D. E.: *J. Appl. Phys.*, **90**, 3509-3515 (2001)
[21] Leapman, R. D. and Sun, S.: *Ultramicroscopy*, **59**, 71-79 (1995)
[22] Hashlmoto, A., Suenaga, K., Gloter, A., Urlta, K. and Iijima, S.: *Nature*, **430**, 870-873 (2004)
[23] Lu, D., Li, Y., Rotkin, S, V., Ravaioli, U., and Schulten, K.: *Nato Lett.*, in press, (2004)

A Study of Metal Nanowire Structures by High-Resolution Transmission Electron Microscopy

Yoshifumi Oshima

Department of Materials Science and Engineering, Tokyo Institute of Technology

Recent research by Kondo and Takayanagi et al. has found that gold nanowires less than 2 nm in diameter have a helical multishell (HMS) structure. Theoretical studies suggest that metal nanowires form a helical structure when synthesized at the atomic level. However, the structures of other metal nanowires have hardly been studied. In addition, single-wall nanotube structures like carbon nanotubes (CNTs) have not been found yet. This study was intended to synthesize platinum and gold nanowires less than 1 nm in diameter in an ultrahigh-vacuum transmission electron microscope (UHV-TEM), and to reveal their structures. Platinum nanowires, which were synthesized at 700 K, showed a HMS structure as in the case of gold nanowires. Further thinning of the platinum nanowires removed the outer tube of the 13-6 HMS structure, and synthesized a single-wall nanotube composed of six atomic rows. Gold nanowires showed a HMS structure when synthesized at 150 K, as they did when synthesized at room temperature. Cooling the gold nanowires to 150 K made the 7-1 gold nanowire thinner, and created a gold nanotube composed of five atomic rows. Further thinning reduced the five atomic rows of the single-wall gold nanotube into a strand of gold atoms as if the nanotube had unraveled.

Introduction

Recent research has discovered conductance quantization of metal nanowires, and it has been drawing much attention. In particular, researchers have observed that alkali metals such as lithium, sodium, and potassium [1-3], and noble metals such as gold, silver, and copper [4-7], show intense peaks in steps of a quantized conductance unit ($G_0=2e^2/h$) in conductance histograms even at room temperature. Since then, the structure of these metals and the mechanism of their electric conductance have been under both experimental and theoretical investigation. As a result, most researchers agree that the structure which corresponds to a unit conductance $G=1G_0$ is a single-atom contact or a single strand of atoms. These metals are monovalent; thus, one s-electron contributes to electric conductance. Therefore, in a single-atom contact, one channel made by a single s-electron contributes to electric conductance [8-10].

On the other hand, single-atom contacts of other metals do not show an intense peak at $G=1G_0$ in conductance histograms. For example, the peaks of aluminum nanowires appear at lower places than the integral multiples of a unit conductance [8, 11]. Also, the conductance of aluminum nanowires tends to increase in the process of stretching the wire, suggesting that the conductance is sensitive to the wire structures. This is considered to be due to the fact that not only s-electrons but also p-electrons contribute to electric conductance in aluminum nanowires, and that the conductance of p-electrons is sensitive to the atomic arrangement and interatomic distance [12, 13]. And in a platinum single atom contact, where d-electrons may contribute to electric conductance, nonlinearity is observed in the I-V characteristics [14]. This is supposedly because the transmission rate of the conductance channel of d-electrons depends on the bias applied to the contact.

In sum, electric conductance in a single atom contact or a strand of atoms reflects the characteristics of each element [3]. The conventional mesoscopic theories cannot explain this phenomenon.

Now let us take a look at the electric conductance of a metal nanowire that consists of two or more atomic rows. Experimental and theoretical reports suggest that a gold nanowire composed of two atomic rows shows conductance of $2G_0$ [9,15] or $1.75G_0$ [16]. There are three metastable structures that have been investigated for the two-atomic-row gold nanowire: ladder geometry, zigzag geometry with strong connections within each atomic row, and zigzag geometry with strong connections between the two rows. Theoretical calculation indicates that the conductance in zigzag geometry shows $2G_0$ or $1G_0$ depending on the connections in the two rows [15].

Moreover, the conductance of thicker alkali metal nanowires can be explained using a shell structure model [2]. A shell structure model is used to illustrate the stable structure of a metal cluster or an atom, which confines electrons within [17, 18]. In this model, when an atom or a cluster has a specific number of electrons to fill the shells such as 1s and 1p, which is defined by the confining potential, that is, when an atom or a cluster has a specific atomic number, the atom or the cluster is a stable structure. These specific numbers are called magic numbers. In metal nanowires, electrons are confined within the cross-sectional plane, and their electric eigenstates are discrete. Because the eigenstates which are below the Fermi energy contribute to the electric conductance, the conductance changes discontinuously depending on the diameter of the nanowire. In a cylindrical nanowire, its conductance takes the values 1, 3, 5, 6, 8, and 10 G_0 due to the degeneracy of the eigenstates. These numbers are called magic numbers [2]. These magic numbers are confirmed in alkali metals such as lithium, sodium, and potassium. However, they are not observed in noble metals such as gold, silver, and copper, which are the same s-electron metals as the alkali metals.

Many experiments have been conducted to measure the electric conductance of various metal and semiconducting nanowires, and conductance histograms have been created. As was discussed earlier, researchers have a good understanding of the properties of an atomic contact and an atomic chain which correspond to the first peak in the conductance histogram [3]. However, little has been discussed for thicker nanowires, their stable structures and their electric conductance mechanism.

Kondo and Takayanagi have recently discovered that gold nanowires with a diameter of less than 2 nm form a helical multishell (HMS) structure [19]. **Figure 1** illustrates the structures of HMS nanowires. The *n*-*m*-*l* HMS nanowire consists of three coaxial tubes. The outer tube has *n* atomic rows, the middle *m* rows, and the inner *l* rows. These atomic rows coil around the tube axis. **Figure 2** shows a sheet of atoms that forms a tube of the HMS nanowire. The sheet has a triangular network of

J1-3, 4259 Nagatsuta, Midori-ku, Yokohama 226-8502, Japan
E-mail: ohshima@materia.titech.ac.jp

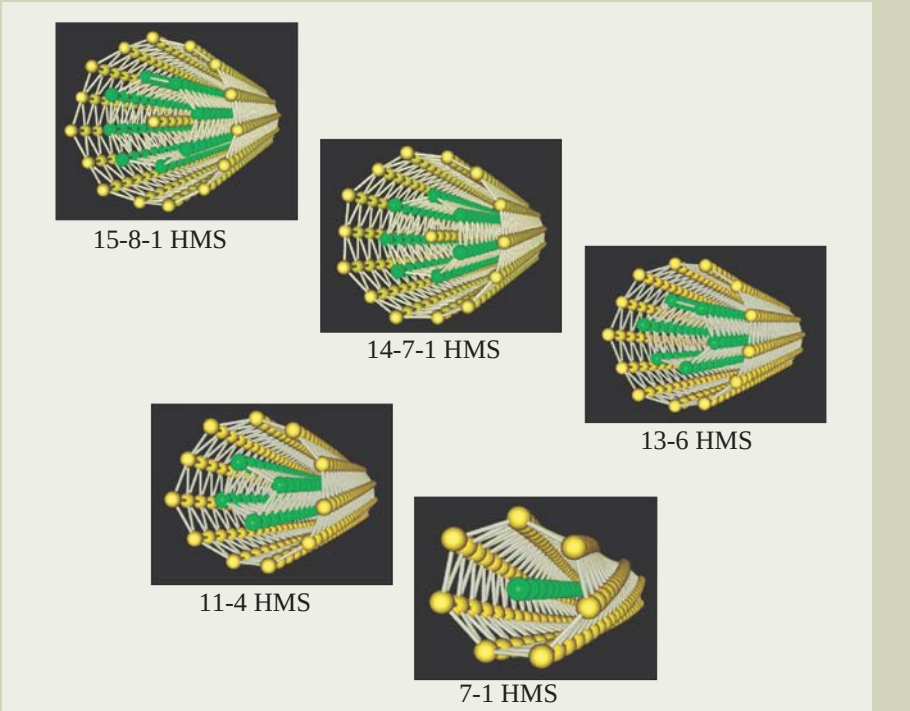

Fig. 1 Models of the gold helical multishell (HMS) structure. The numbers n, m, and l in *n-m-l* HMS refer to the number of atomic rows in the outer, middle, and inner shells, respectively. The difference in the number between the two adjacent shells is 7, the magic number.

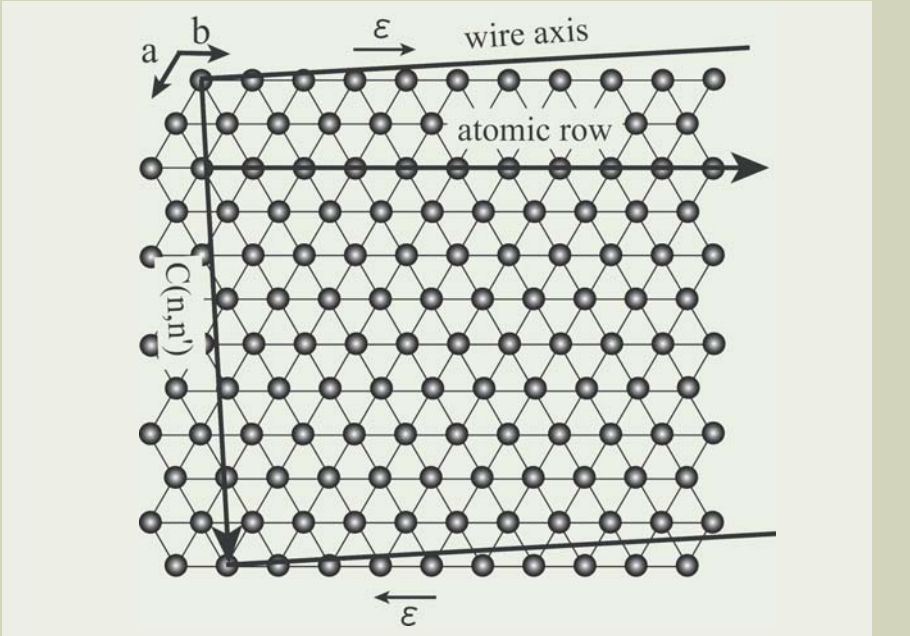

Fig. 2 A sheet of atoms that constitute a tube of a HMS nanowire. The atoms are in a triangular network which coils around the wire axis to form a tube. The atomic row corresponds to the atoms lined up along the [110] direction. C (n, n') is the chiral vector, and the direction perpendicular to the chiral vector is the wire axis.

atoms, and the atomic row corresponds to the atoms lined up along the [110] orientation indicated by the arrow. The atomic geometry of the HMS nanowire resembles that of the multiwall carbon nanotube, except for a few differences. The carbon nanotube has a honeycomb network in the sheet of atoms, while the gold HMS nanowire has a triangular network. Also, the triangular network is deformed by the shear strain ε in the direction of the atomic rows. Furthermore, in the gold HMS nanowire, the difference of the numbers of atomic rows between the two adjacent tubes is always 7, the magic number. This magic number can be explained by taking the nearest neighbor atom distance of gold into consideration, which provides strong evidence to support the structural model of the nanowires [19].

The characteristics of HMS nanowires can be defined by two physical values: the chiral vector and the helical pitch [19, 20]. The chiral vector corresponds to the circumference of each tube, and is indicated by C (n, n') as in **Fig. 2**. Here, n is the number of atomic rows, and n' is defined as n'=n/2 when n is an even number, and as n'=(n+1)/2 when n is an odd number. The helical pitch is given by L=|C (n,n')|/tan θ, where θ is the angle between the atomic row and the tube axis. Note that |C (n, n')| and θ depend on the shear strain ε in the atomic row direction. The chiral vector and helical pitch can be measured using a high-resolution transmission electron microscope image.

The helical structure of metal nanowires is theoretically supported as well. Tosatti *et al*. predicted that the helical structure becomes stable when a nanowire is a certain critical diameter or less, based on the detailed study of the structures of lead and aluminum nanowires [21, 22]. Also, Bilalbegović reported that gold nanowires form a multiwall tubular structure [23]. However, the gold HMS structure is the only known helical structure to date.

This present study investigates whether metal nanowires other than gold can have a helical structure, and suggests the possibility of single-wall metal nanotubes like carbon. This article discusses synthesizing and studying the structure of 1) platinum nanowires, and 2) single-wall gold nanotubes.

Experiment

In this study, we used JEOL JEM-2000FXV [24] and JEM-2000VF Ultrahigh-Vacuum Transmission Electron Microscopes (UHV-TEM). To investigate physical properties at the atomic level, it is necessary to remove the influence of contamination. For observation of platinum nanowires, we used a JEOL specimen-heating holder, which can keep the specimen at any temperature between room temperature and 1000°C in ultrahigh vacuum. The holder has a two-axis tilting capability, which is suitable for high-resolution observation. For observation of gold nanowires, on the other hand, we used our original liquid-nitrogen specimen-cooling holder, which can keep the specimen at several temperatures between room temperature and 150 K.

Results

Platinum nanowires [25]

We synthesized platinum nanowires as follows. We used the Pashley method [26] to prepare a thin film of a platinum (001) single crystal. In an ultrahigh-vacuum chamber, a film of silver about 500 nm thick was predeposited on the (001) cleaved surface of a NaCl single crystal at a substrate temperature of 300°C. Then platinum was coated on the silver film by vacuum deposition. We obtained a (001) platinum film 3-5 nm in thickness by dissolving the NaCl with water and the silver with nitric acid. We mounted the platinum thin film on a holey carbon film, which was supported by a molybdenum microgrid. The EDS analysis of this platinum thin film detected no characteristic X-rays from silver.

The platinum thin film was irradiated with an intense electron beam (300 A/cm^2) while heating the film to 700 K in the UHV-TEM. The pressure in the chamber was below 5 $\times 10^{-8}$ Pa. For observation of the formation of nanowires, we reduced the intensity of the electron beam to 20 A/cm^2, and viewed the thin film through a TV camera installed in the microscope. The acquired images were record-

ed on videotape at 30 ms/frame. **Figure 3** shows (a) a high-resolution image, and (b) a diffraction pattern of the (001) platinum thin film after 6-7 hours of irradiation. The lattice fringes of the observed image agreed with the basic lattice constant of the (001) platinum surface (a=0.277 nm). The contrast of the lattice fringe had modulation with a period of 5 as indicated by the thick white lines, suggesting that the platinum thin film had a superlattice structure with a period of 5. The diffraction pattern shows the reciprocal lattice unit on the (001) platinum surface indexed as (10) and (01) as well as the hexagonal lattice unit indicated by the dashed line. The reciprocal primitive lattice unit and the hexagonal lattice unit coincide at (20), but they are in a 4:5 ratio at (01) and A. This suggests that the superlattice structure conformed to the primitive lattice in the (10) direction, with a period of 5 in the (01) direction. This 1×5 structure is known as the reconstruction of the (001) platinum surface [27, 28]. Therefore, we can interpret that the platinum thin film at this time was almost free of contamination.

Irradiating the platinum thin film with an intense electron beam created many holes. A platinum nanowire was formed between two adjacent holes. After irradiating it with an intense electron beam over 10 hours, we could observe a nanowire about 1 nm in diameter. **Figure 4 (a)** is the acquired TEM image of the platinum nanowire. The five wavy fringes show the characteristic of a HMS nanowire. The apparent width of the nanowire, though it varied from place to place due to its helical structure, was 0.98 nm on average. **Figure 4 (b)** is a TEM image of a typical gold 13-6 HMS nanowire. The diameter of the gold 13-6 HMS nanowire is 1.04 nm, but its apparent width is 0.96 nm. The apparent width of a nanowire obtained from a TEM image differs from its actual diameter. Because of the mechanical vibration of the specimen-heating holder, the resolution of the TEM image of the platinum nanowire was worsened. However, considering that the lattice constant of platinum is almost the same as that of gold, we can assume that this platinum nanowire was a 13-6 HMS nanowire. For comparison, we also simulated images of 11-4, 12-5, 13-6, and 14-7-1 platinum HMS nanowires. Among them, the 13-6 HMS nanowire had the apparent width and fringes closest to those of the obtained TEM image.

As we observed the nanowire further, the outer tube of the HMS nanowire was partially removed and a nanowire with two fringes was observed (**Fig. 5 (a)**). It was caused by diffusion of the atoms which constituted the outer tube toward the electrodes. The nanowire with two fringes remained for 2 to 3 seconds. Its apparent width was 0.4 to 0.45 nm. To compare with the TEM image, we simulated images of 7-1, 6-0, and 5-0 platinum nanowires. The simulated image of a 7-1 HMS nanowire showed three fringes, and its apparent width was 0.52 nm. In the simulated image of a 5-0 HMS nanowire, there were two fringes. Its apparent width was 0.35 nm, which disagreed with the obtained TEM image. On the contrary, the simulated image of a 6-0 HMS nanowire had two fringes, and its apparent width was 0.42 nm, which agreed best with the observation. We also investigated 5-1 and 6-1 HMS nanowires by image simulation, although it was highly unlikely that a tube composed of five or six atomic rows could contain a strand of atoms inside. The simulated image of a 5-1 HMS nanowire showed two fringes that were asymmetric to the wire axis, and the difference in contrast between the two fringes was larger compared to that of the 5-0 HMS nanowire. In the simulated image of a 6-1 HMS nanowire, though there was a contrast of two fringes similar to that of the 6-0 HMS nanowire, it had three fringes in some parts. The two fringes observed in **Fig. 5 (a)** are symmetric to the wire axis with equal contrast. Therefore, we concluded that the simulated image of the 6-0 HMS nanowire best matches the obtained TEM image. **Figure 5 (b)** shows the simulated image of the 6-0 HMS nanowire that corresponds to the TEM image. **Figure 5 (c)** shows a three-dimensional model of the nanowire. A closer

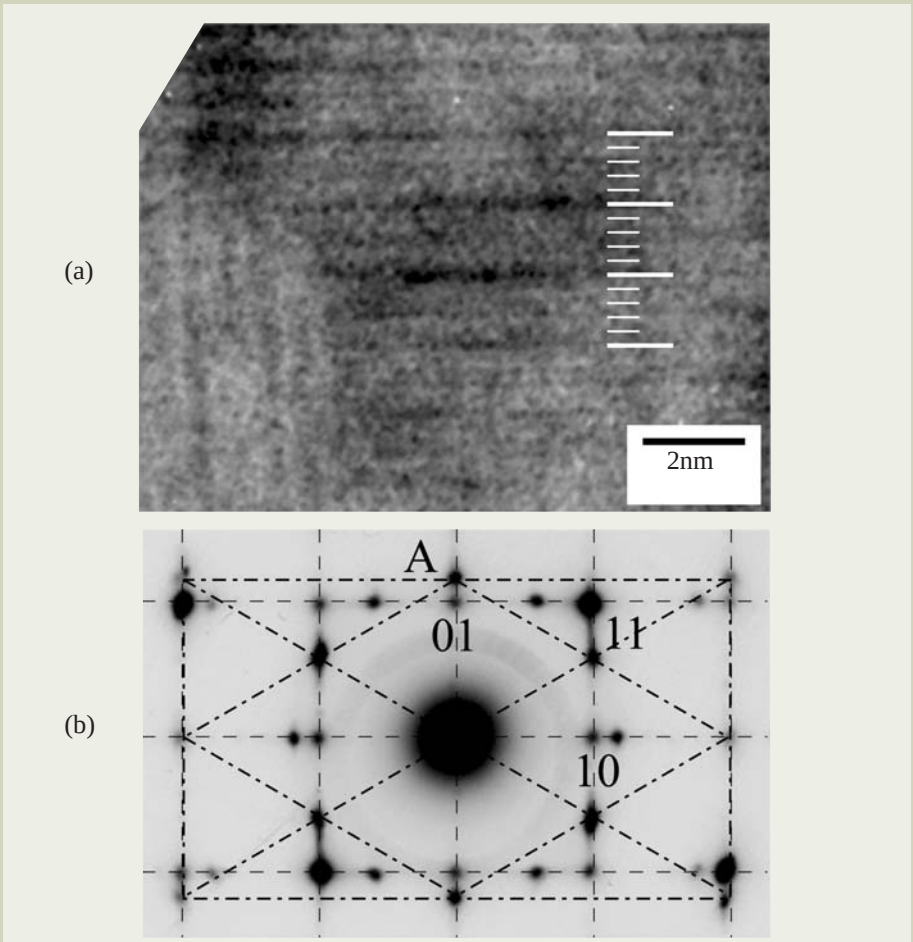

Fig. 3 (a) TEM image and (b) diffraction pattern of the (001) platinum thin film after irradiation with an intense electron beam. The superlattice structure characteristic of the clean (001) platinum surface can be observed.

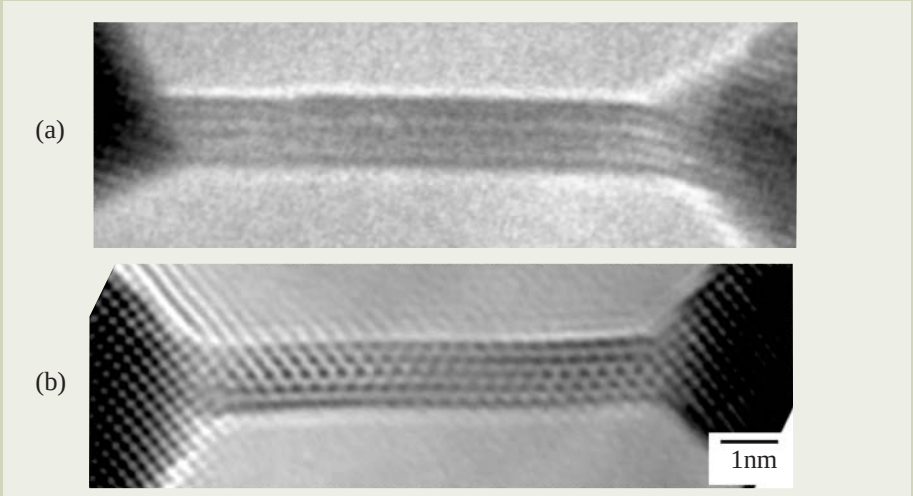

Fig. 4 (a) TEM image of the 13-6 HMS platinum nanowire, and (b) the TEM image of the 13-6 HMS gold nanowire.

look at the images reveals that each of the two fringes observed at the P position is an image of three atomic rows superposed along the direction of the incident electron beam. At the Q position, on the other hand, the two fringes are the images of two superposed atomic rows, and the thin fringe along the center axis is formed with the remaining two atomic rows. Therefore, the observed nanowire was a single-wall nanotube composed of six atomic rows. It was consistent with the fact that this nanotube was formed by removing the outer tube of the 13-6 HMS nanowire.

We could obtain a platinum single-wall nanotube from the 13-6 HMS nanowire. This nanowire persisted for 2 to 3 seconds, which confirmed the formation of a platinum single-wall nanotube. The result implies that a single-wall nanotube composed of five atomic rows might be formed if it is possible to synthesize a single-wall nanotube from a 12-5 HMS nanowire.

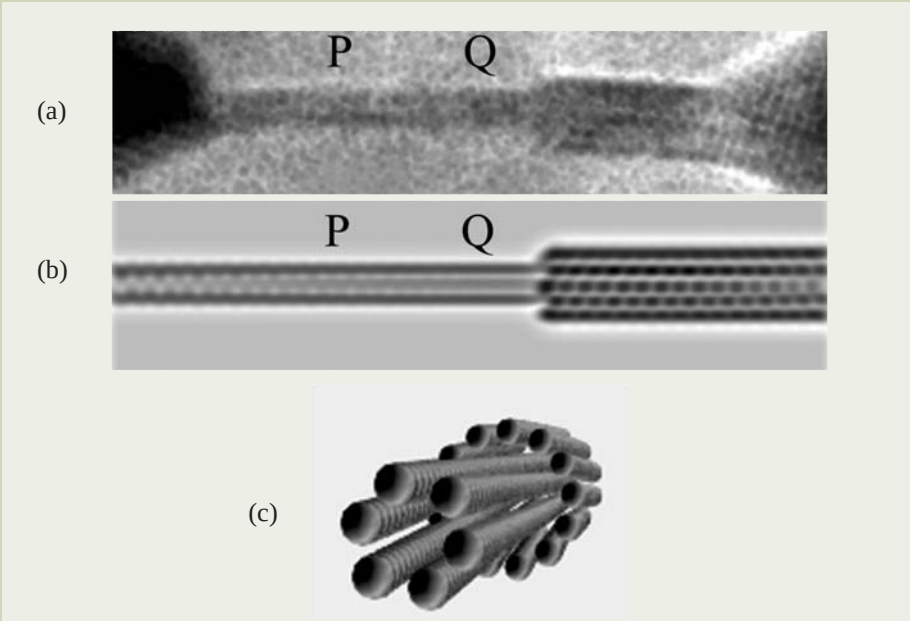

Fig. 5 (a) TEM image of the platinum single-wall nanotube formed after the outer tube of the 13-6 HMS platinum nanowire was removed, (b) simulated image of the single-wall nanotube composed of six atomic rows connected to the 13-6 HMS, and (c) model structure of the single-wall nanotube composed of six atomic rows connected to the 13-6 HMS.

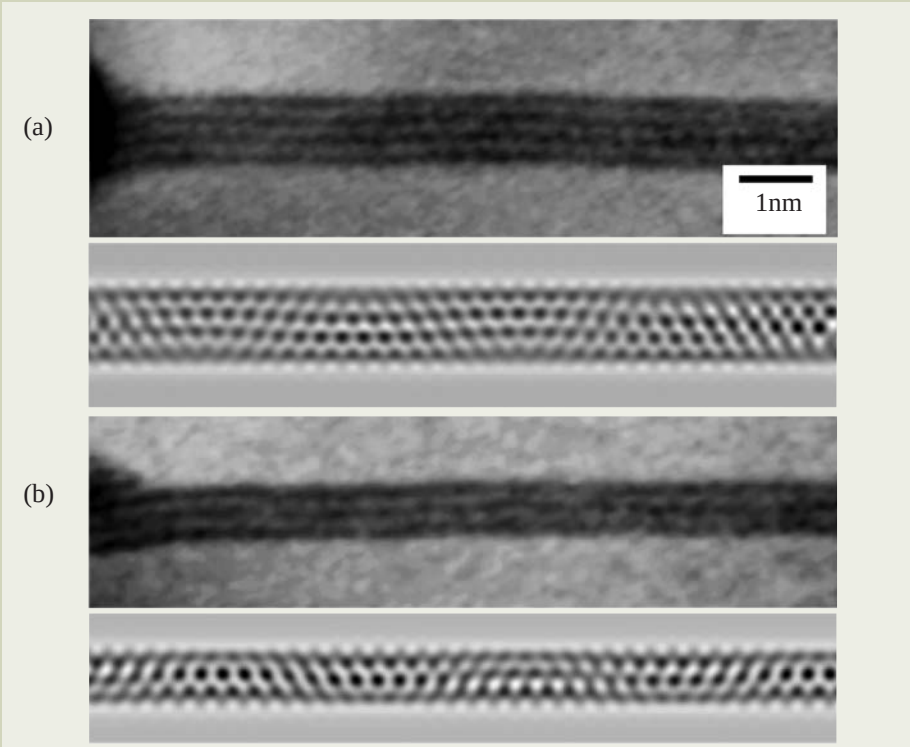

Fig. 6 TEM images and simulated images of HMS gold nanowires synthesized at 150 K. (a) 13-6 HMS, and (b) 11-4 HMS.

Single-wall gold nanowires [20]

The thinnest gold HMS nanowire that has ever been observed at room temperature is a 7-1 HMS nanowire (see **Fig. 1**). A single-wall gold nanotube has yet to be found. The gold HMS nanowires change their structure from the 14-7-1 HMS structure to the 13-6, 12-5, and 11-4 HMS structures through thinning [19]. This change is accompanied by dynamic processes such as diffusion and rearrangement of atoms. The speed of atomic diffusion slows down as the temperature of the specimen becomes lower. So we experimented to control the intense movement of atoms by cooling the specimen. This way, the 7-1 HMS nanowire may turn into a single-wall nanotube or a strand of atoms without breaking.

Irradiating a (001) gold thin film with an intense electron beam formed many holes, and a nanowire was created between two adjacent holes. We prepared a (001) single-crystal gold thin film using the Pashley method as we did earlier with the platinum thin film. The thickness of the film was about 2 nm. Then, we mounted the gold thin film on a holey carbon film, which was supported by a molybdenum microgrid. The thin film was irradiated with an intense electron beam of 300 A/cm^2 in the UHV-TEM at room temperature. The pressure at this time was 1×10^{-7} Pa or lower. After a few hours of irradiation, the surface of the thin film was cleaned up, and many holes were formed on the thin film. Further irradiation expanded the holes, and the area between two adjacent holes became a nanowire. At this time, we cooled the specimen to 150 K, and lowered the intensity of the electron beam irradiation to 50 A/cm^2. When the nanowire became less than 2 nm wide, we lowered the intensity of the electron beam irradiation to 30 A/cm^2, and recorded the change in the structure of the nanowire through a TV camera on videotape at 30 ms/frame.

The gold nanowires formed at 150 K had the same HMS structure as those observed at room temperature. By cooling the specimen to 150 K, we could observe thin nanowires such as 7-1 HMS more frequently than at room temperature. We could obtain nanowires longer than 10 nm more frequently as well. **Figure 6** is the TEM image of a typical gold nanowire synthesized at 150 K. **Figure 6 (a)** shows four wavy fringes. These wavy lines are the characteristic pattern in the TEM image of a HMS nanowire. We can calculate the helical pitch using this pattern. The apparent width of the nanowire was 0.8 nm. Further thinning of this nanowire formed another nanowire shown in **Fig. 6 (b)**. This nanowire had three wavy fringes, and its apparent width was 0.56 nm. **Figures 6 (a)** and **(b)** include simulated images of the 11-4 HMS and 7-1 HMS nanowires. The simulated images reproduce the obtained TEM images precisely, confirming the formation of the 11-4 HMS and 7-1 HMS nanowires. As shown in **Fig. 6**, one pitch of the wavy fringe corresponds to L/n in the n-m-l HMS nanowire. The helical pitches of the two nanowires were 65-75 nm and 26-28 nm, respectively. The 11-4 HMS and 7-1 HMS nanowires synthesized at room temperature had helical pitches of 84 nm and 28 nm, respective-

ly [19]. Thus, the helical pitch of the nanowires formed at 150 K was smaller, but the difference does not seem significant.

Figure 7 shows the process of further thinning of the gold nanowire. The TEM images of the nanowire showed two fringes in **Fig. 7 (a)**, and one fringe in **Fig. 7 (b)**. The former nanowire was present for about 10 seconds, and the latter for about 1 second. We could observe similar images with one or two fringes rather frequently. The apparent width of the nanowire with two fringes was 0.25 nm on average, which is thinner than a 7-1 HMS nanowire. So we simulated images of a 6-0 HMS, 5-0 HMS, 4-0 HMS, 3-0 HMS and zigzag nanowire composed of two atomic rows, and compared them with the TEM images. The simulated images of the 5-0 HMS and zigzag nanowire composed of two atomic rows showed the apparent width closest to the observed TEM images. **Figure 8 (a)** is a high-resolution TEM image of the nanowire with two fringes. The direction of the fringes that run diagonally across the nanowire inverts every 4 or 5 atoms along the atomic row. **Figures 8 (b)** and **(c)** are the model of a 5-0 HMS and its simulated image. The pattern of the fringes that run diagonally across the nanowire agrees well with that of the TEM image. Thus, this nanowire is a single-wall gold nanotube composed of five atomic rows, which has the 5-0 HMS structure. The single-wall nanotube turned into one fringe in about 10 seconds as shown in **Fig. 7 (b)**, as if the five atomic rows unraveled themselves. The TEM image showed a 3 nm long strand of 11 gold atoms. In such a single strand, it seemed that the atoms fluctuated so much that their positions were not determined precisely. Sen *et al.* argue for the stability of a gold pentagonal nanowire [29]. Although their model is different from ours, they suggest that a hollow tubular wire structure is stable.

Conclusion

This study investigated the structures of platinum and gold nanowires using a UHV-TEM. We successfully synthesized platinum nanowires at 700 K by irradiating a platinum (001) thin film 2-4 nm in thickness with an intense electron beam. The platinum nanowires formed a HMS structure like gold nanowires as their diameter became smaller. Further thinning by irradiation with a weak electron beam removed the outer tube of the 13-6 HMS nanowire and provided a single-wall nanotube composed of six atomic rows. Moreover, we succeeded in synthesizing a single-wall gold nanotube by cooling the specimen to 150 K. The gold nanowire synthesized at 150 K had the same HMS structure as that synthesized at room temperature. Further thinning reduced the 7-1 HMS nanowire into a single-wall nanotube composed of five atomic rows. The single-wall nanotube turned into a strand of 11 atoms as if the atomic rows that constituted the nanotube unraveled themselves.

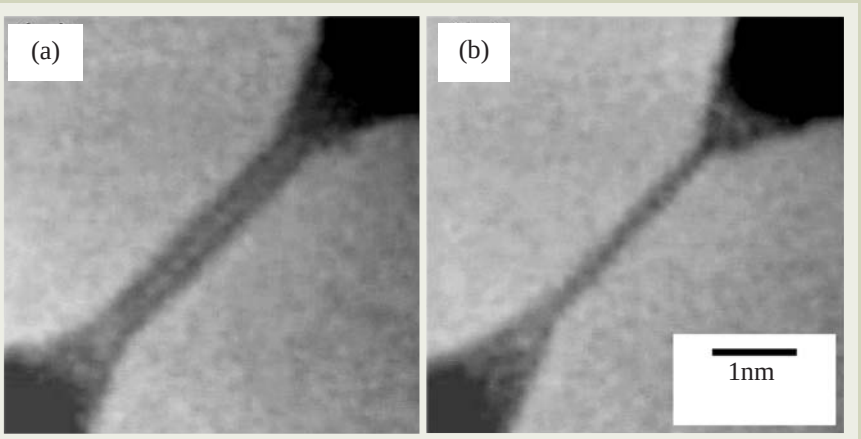

Fig. 7 (a) TEM image of a nanowire with two fringes, and (b) TEM image of a nanowire with one fringe, observed during the thinning process.

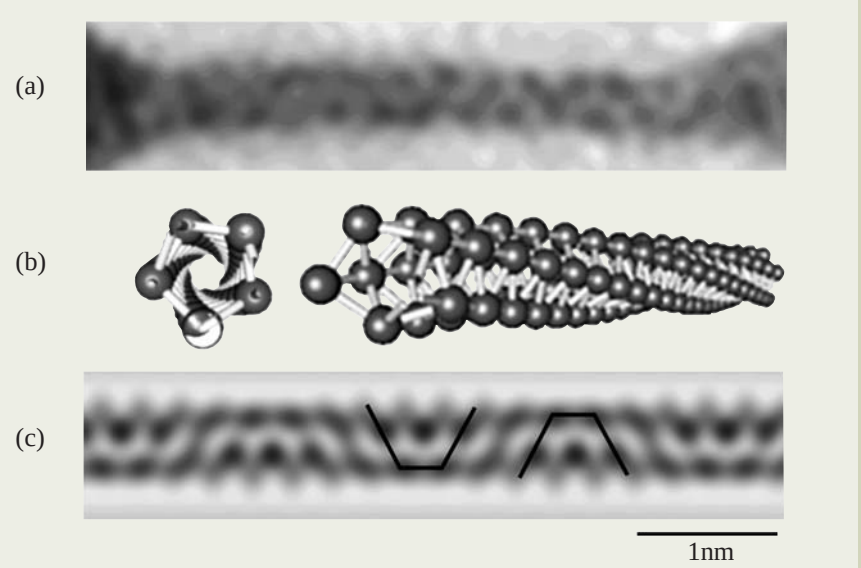

Fig. 8 (a) TEM image of the single-wall nanotube composed of five atomic rows, (b) model structure of the nanotube, and (c) simulated image of the nanotube.

References

[1] J. M. Krans et al., *Nature* **375**, 767 (1995)
[2] A. I. Yanson, I. K. Yanson and J.M. van Ruitenbeek, *Nature* **400**, 144 (1999)
[3] N. Agrait, A. L. Yeyati and J. M. van Ruitenbeek, *Phys. Rep.* **377**, 81 (2003)
[4] M. Brandbyge, J. Schioyz et al., *Phys. Rev.* **B 52**, 8499 (1995)
[5] C. J. Muller et al., *Phys. Rev.* **B 53**, 1022 (1996)
[6] J. L. Costa-Kramer, N. Garcia and H. Olin, *Phys. Rev.* **B 55**, 12910 (1997)
[7] K. Hansen, et al., *Phys. Rev.* **B 56**, 2208 (1997)
[8] E. Scheer et al., *Nature* **394**, 154 (1998)
[9] H. Ohnishi, Y. Kondo and K. Takayanagi, *Nature* **395**, 780 (1998)
[10] A. I. Yanson, et al., *Nature* **395**, 783 (1998)
[11] J. M. Krans et al., *Phys. Rev.* **B 48**, 14721 (1993)
[12] P. Jelinek et al., *Phys. Rev.* **B 68**, 085403 (2003)
[13] S. Okano, K. Shiraishi and A. Oshiyama, *Phys. Rev.* **B 69**, 045401 (2004)
[14] S. K. Nielsen et al., *Phys. Rev. Lett.* **89**, 066804 (2002)
[15] J. Nakamura, et al., *Surf. Sci.* **482-485**, 1266 (2001)
[16] B. Ludoph, et al., *Phys. Rev. Lett.* **82**, 1530 (1999)
[17] W. A. de Haar, Rev. Mod. Phys. 65, 611 (1993)
[18] M. Brack, *Rev. Mod. Phys.* **65**, 677 (1993).
[19] Y. Kondo and K. Takayanagi, *Science* **289**, 606 (2000)
[20] Y. Oshima, A. Onga and K. Takayanagi, *Phys. Rev. Lett.* **91**, 205503 (2003)
[21] O. Gülseren, F. Ercolessi and E. Tosatti, *Phys. Rev. Lett.* **80**, 3775 (1998)
[22] E. Tosatti et al. *Science* **291**, 288 (2001)
[23] G. Bilalbegović , *Phys. Rev.* **B 58**, 15412 (1998)
[24] K. Takayanagi, Y. Tanishiro, K. Kobayashi, K. Akiyama and K. Yagi, *Jpn. J. Appl .Phys.* **26**, L957 (1987)
[25] Y. Oshima, H. Koizumi, K. Mouri, H. Hirayama, Y. Kondo and K. Takayanagi, *Phys. Rev.* **B 65**, 121401(R) (2002)
[26] D. W. Pashley, *Adv. Phys.* **5**, 173 (1956)
[27] M. A. van Hove et al., *Surf. Sci.* **103**, 189 (1981)
[28] D. Gibbs et al., *Phys. Rev. Lett.* **67**, 3117 (1991)
[29] P. Sen, O. Gülseren, T. Yildirim, I.P.Batra and S. Ciraci, *Phys. Rev.* **B 65**, 235433 (2002)

Introduction of JWS-2000 Review SEM

Yoshiyuki Eto and Tomohiro Mihira

Technical Division, JEOL Ltd.

Introduction

Yield management of each process is becoming more important with shrinkage of semiconductor devices, introduction of new materials into semiconductor-production lines, and increase in the number of processes. The review SEM is a scanning electron microscope (SEM) for observing defects and surface shapes of semiconductor devices without cleaving wafers. It is now an indispensable tool for yield management.

To increase the efficiency of defect review, the review SEM is required to achieve automatic operation and high-throughput operation. We have developed the JWS-2000, a new review SEM that meets these requirements. The JWS-2000 is a successor to the JWS-7500 series, which have been used by many users. The external view of the JWS-2000 is shown in **Fig. 1.**

The JWS-2000 is compatible with wafers 200 mm or less in size and can observe the entire surface of a wafer, tilted up to 60°. In addition, the JWS-2000 has various functions such as high-throughput inline automatic defect review (ADR), tilt ADR and automatic energy-dispersive X-ray spectrometry (EDS), which are enabled by a wafer-height sensor and a high-speed stage. The features of the JWS-2000 are presented below.

Features of JWS-2000

Wafer-height sensor

A wafer-height sensor monitors wafer height. The JWS-2000 comes with this height sensor, making it possible to offer the following two capabilities: 1) tilt ADR and 2) bare-wafer ADR.

●Tilt ADR

When the wafer is tilted, stage-positioning accuracy is degraded due to the height distribution of the wafer surface in previous review SEMs (**Fig. 2a**). This made tilt ADR difficult because it was impossible to increase the initial magnification. To break through this limitation, the JWS-2000 uses the wafer-height information for stage-position correction. This new feature has achieved a high stage-positioning accuracy during tilt ADR, comparable to that of flat ADR (**Fig. 2b**). Thus, the JWS-2000 can perform tilt ADR without lowering magnification, and detects micro-defects as small as those during flat ADR. Tilting the stage enables one to obtain 3D shape information on defects, which are difficult to confirm by top-view observation **(Fig. 3).**

●Bare-wafer ADR

A bare wafer or a sample (wafer) with a very flat surface provides weak SEM image contrast, making it difficult to focus exactly on the wafer surface. To solve this problem, we have introduced a new method that feeds back height information from the height sensor to focusing. The height sensor corrects variations in focus by height changes. In addition, height information is calibrated using the built-in standard sample. Since the focusing problem has been solved, ADR for bare wafers or flat-surface samples has become possible (**Fig 4**).

Focusing during manual observation is also possible using the height sensor. It facilitates observation of micro-defects such as crystal originated particles (COP).

AFC (auto focus control)

To enhance the auto focus control (AFC) accuracy, the JWS-2000 comes with the AFC function using image processing. Combining this improved AFC with the height sensor enables one to carry out high-performance ADR.

High-throughput ADR

The JWS-2000 has increased the ADR throughput by making stage movement faster and optimizing communication protocols, etc. The ADR throughput of previous instruments was 400 DPH (defects per hour). The JWS-2000 offers a higher ADR throughput of 600 DPH. (ADR throughput is measured under the following conditions: Measurement mode: die to die, During acquisition of defect-enlarged images, Sample: JEOL standard wafer.)

Automatic EDS

A review SEM must perform element analysis automatically, in order to meet users' needs. To do this, the JWS-2000 has made it possible to carry out automatic EDS that combines EDS and ADR. The JWS-2000 can automatically detect defects and acquire EDS spectra (**Figs. 5 and 6**).

ADC (automatic defect classification)

For ADC, the JWS-2000 uses four detectors (right, left, upper and lower) that are highly

Fig. 1 External view of the JWS-2000.

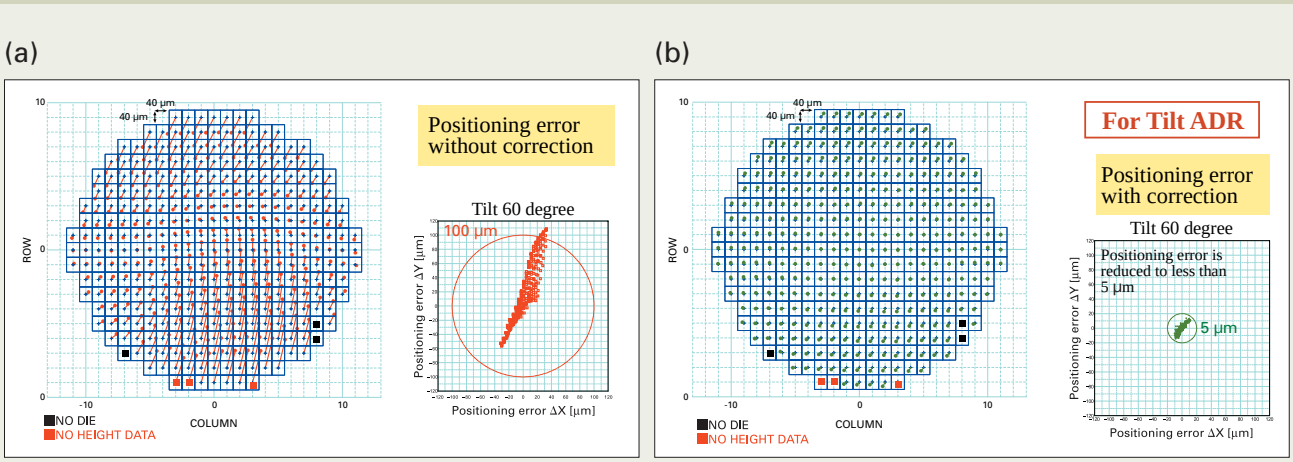

Fig. 2 Stage-positioning accuracy. (a) without height-mapping position correction and (b) with height-mapping position correction.

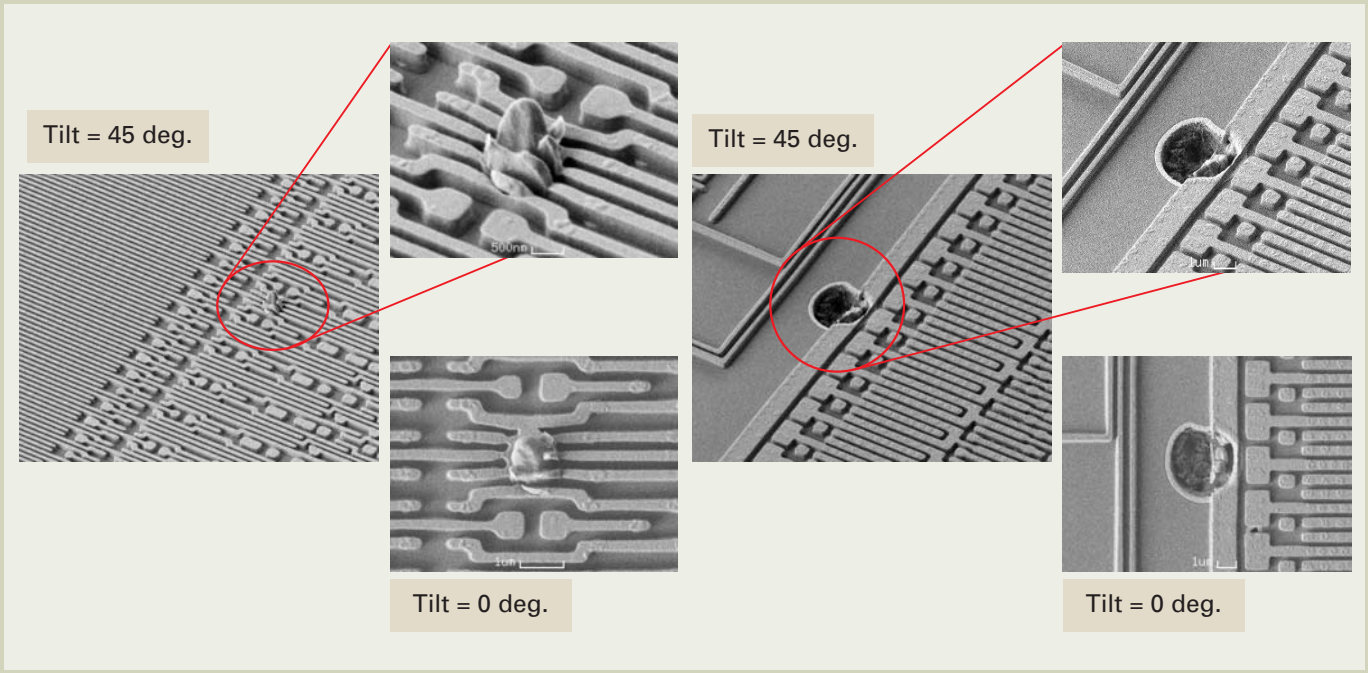

Fig. 3 Examples of tilt ADR and flat ADR.

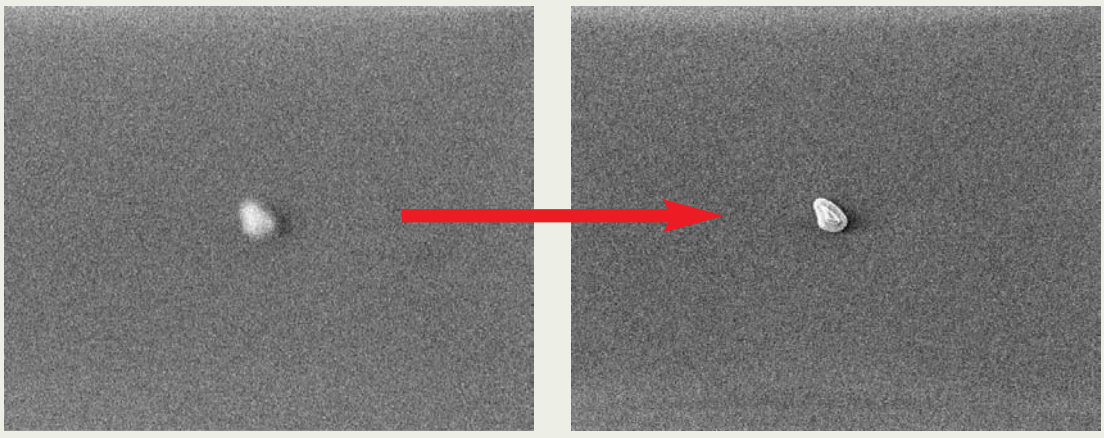

Fig. 4 Effectiveness of focus control using the height sensor (without control (left) and with control (right)).

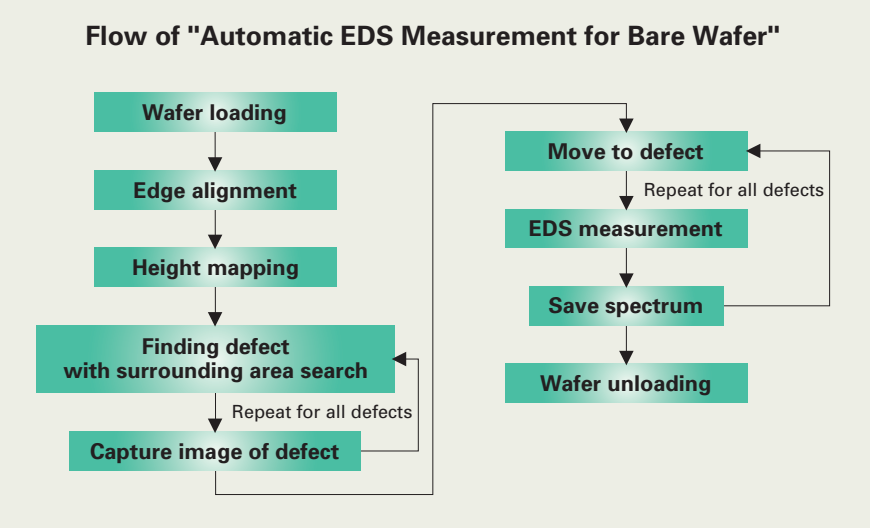

Fig. 5 Flow of automatic EDS.

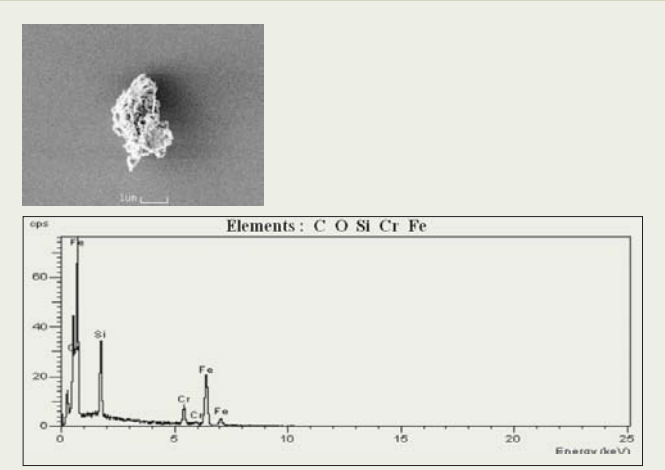

Fig. 6 Example of automatic EDS result.

regarded in the JWS-7555S. Eight basic classifications, based on information obtained from secondary-electron (SEM) images, are available. These ADR classifications can be shared for each layer. Since this basic classification has high accuracy even though it is learningless, it is possible to perform smooth ADC operation.

For detailed classification, based on those eight classifications, necessary classification items can be selected from the factory-prepared list of seventy items. The selected items can be defined as a user classification.

Improvement of SEM image quality

Placing an electrode on the JWS-2000 objective lens has improved the SEM image quality during tilt observation. The higher image quality enables one to observe in more detail the contrast difference due to pattern roughness or the difference in material (**Fig. 7**).

Charge-reduction

The JWS-2000 has added the charge-reduction function for clearly imaging samples susceptible to charging (**Fig. 8**).

Summary

We have briefly explained the JWS-2000 review SEM. This review SEM has improved automatic-observation functions in addition to the highly regarded manual observation of the JWS series. The JWS-2000 will be expected to play a more important role in yield management of semiconductor devices.

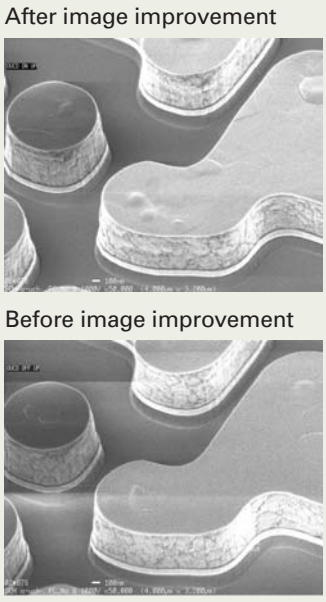

Fig. 7 Improvement of SEM image quality.

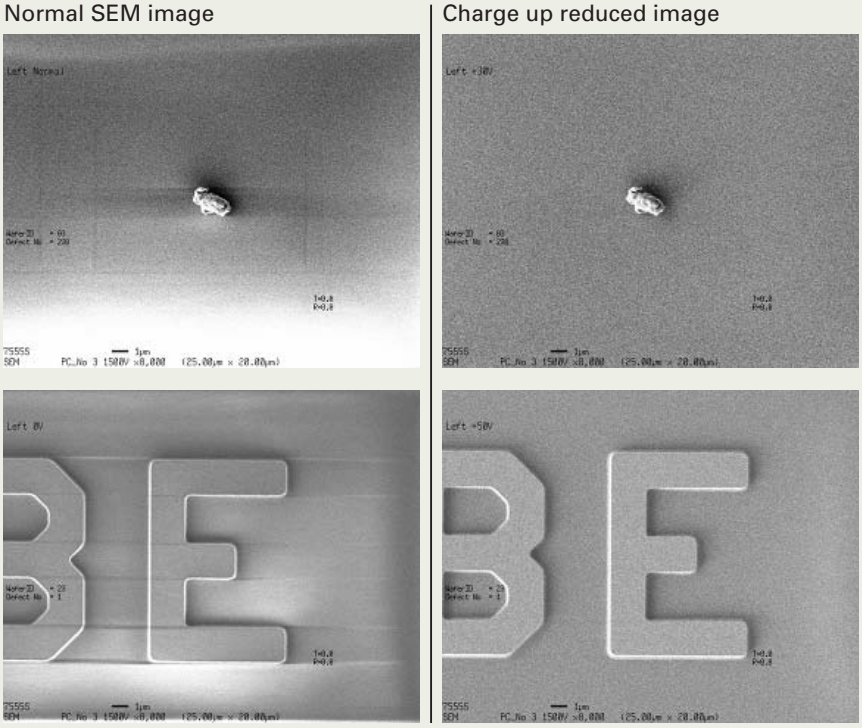

Fig. 8 Charge-reduction function.

Grazing-Exit Electron Probe Microanalysis (GE-EPMA)

Kouichi Tsuji

Graduate School of Engineering, Osaka City University, PRESTO, JST

Introduction

Electron probe microanalysis (EPMA or SEM-EDS) is an indispensable analytical method for materials development or various inspections. The electron probe microanalyzer (EPMA), a general-purpose surface analyzer, allows observation of surface shapes of specimens using a finely focused electron beam. It can also perform qualitative and quantitative analysis of constituent elements in the specimen by detecting characteristic X-rays emitted from the specimen irradiated with the electron beam. The X-ray generation occurs in a region measuring several micrometers deep in many cases, as will be explained later. Since this can be regarded as a local region, the EPMA can offer micro-area element (qualitative) analysis. In addition, various correction methods have been devised for quantitative analysis through many studies so far, making it possible for the EPMA to provide highly accurate quantitative analysis. Furthermore, improvements in analytical software and the method of operating the EPMA have made it easy to use.

On the other hand, the EPMA has several demerits: a) the specimen is susceptible to damage due to electron-beam irradiation, b) the specimen has to be placed in vacuum, c) the analysis region is of the order of micrometers (not nanometers), d) it is difficult to analyze micro-volume specimens. To overcome demerits a) and b), the low-vacuum SEM and the environmental SEM have been developed, and with these developments, the application fields of the EPMA have broadened.

As shown in **Fig. 1 (a)**, since an electron beam is scattered by a solid specimen, even when the diameter of the electron beam irradiating the specimen surface is only several tens of nanometers, the characteristic X-rays emitted by the specimen come from a region several micrometers in depth within the specimen. As miniaturization of semiconductor devices and research on nano-science increasingly advance, analysis of a very minute region is increasingly required. Thus, although several-micrometer-order analysis may meet users' needs depending on the type of specimens, measures to support analysis of smaller regions are needed. Since the analysis depth depends on the accelerating voltage of the electron beam, the application of low accelerating voltages limits the characteristic-X-ray generation region to a minute region near the specimen surface. However, the energies of the X-rays are less than those of the accelerated electrons; this causes a new problem: the use of analytical X-ray lines is limited. This is particularly serious for SEM-EDS that has low energy resolution. The next section introduces the grazing-exit X-ray analysis method, which has the possibility for improving the analysis region and micro-volume analysis.

Sugimoto 3-3-138, Sumiyoshi-ku, Osaka 558-8585, Japan
E-mail : tsuji@a-chem.eng.osaka-cu.ac.jp

Grazing-Exit X-ray Analysis

In many cases, conventional EPMA or SEM-EDS detects characteristic X-rays with a relatively large take-off angle of 30 to 45°. In particular, an EDS detector is placed as near as possible to the specimen so that the X-rays are measured with a larger solid angle. Thus, the analysis depth extends to the order of micrometers, as shown in **Fig. 1 (a)**. Let me repeat that many specimens afford such a micrometer-order deep analysis, making EPMA a useful method for localized analysis. However, if it is necessary to obtain information on the region from the surface to a depth of a few nanometers, conventional EPMA has difficulty in analyzing this limited region. A method to break through this obstacle is grazing-exit X-ray analysis, which measures X-rays at very small take-off (grazing-exit) angles from the specimen surface, as shown in **Fig. 1 (b)** [1-4]. To limit the solid angle, a slit is attached between the specimen and the detector, actually, on the top of the EDX detector. This instrument layout enables one to measure only characteristic X-rays emitted from the near-surface regions: that is, the X-rays emitted from the deep regions are not detected by the EDX detector due to strong X-ray absorption in the specimen and refraction effects at the specimen surface (**Fig. 2**). Compared to conventional EPMA, the intensity of the detected X-rays is lower; however, an important point for surface analysis is the ratio of the signal intensity from the surface to that from the bulk. The grazing-exit analysis (**Fig. 2**) greatly enhances surface sensitivity in X-ray measurement. For the instrument configuration needed for this grazing-exit analysis, refer to different papers [3, 5, 6].

In this method, precise take-off (exit) angle control is of crucial importance. To put it simply, this is achieved by tilting the specimen stage in the direction of the X-ray detector [6]. Another way of doing this is to move the X-ray detector or the specimen stage up and down [5, 7]. For providing a slit, two pieces of metal are affixed on the top of the EDX detector, or an aperture is placed between the specimen and the detector. Therefore, a special device is not needed and one can perform grazing-exit X-ray analysis using a commercial EPMA or SEM-EDS.

Application Examples of Grazing-Exit X-ray Analysis to EPMA

Surface analysis

Figure 3 shows the dependence of the analysis depth on exit angle for characteristic X-rays (in this case, SiKα from a silicon wafer) [1, 2]. It is shown that a certain critical angle exists, and that the analysis depth becomes as shallow as a few nanometers at angles below the critical angle. Thus, it is possible to perform surface analysis by setting the exit angle to this range of angles and by measuring the X-rays. Although it is not easy to precisely determine the critical angle, when X-ray measurement or mapping measurement is carried out while the specimen is tilted to decrease the exit angle, the intensity of characteristic X-rays changes at a certain angle, showing the transitional behavior from bulk analysis to surface analysis. **Figure 4** shows an example of observation of the contamination on a specimen surface using the grazing-exit X-ray analysis [8]. It is found that the contamination on the surface is well observed with high sensitivity at small exit angles, which was not realized at conventional large exit angles.

Reduction of background

An important point for observation and analysis of trace components is signal-to-background intensity ratio (S/B ratio), that is, the enhancement of the ratio of the signal intensity of characteristic X-rays to the background

Table 1 Analysis regions within the specimen estimated by Monte Carlo simulation of electron trajectories (unit: nm)
(The horizontal arrow in Fig. 1 indicates the size.)

		Electron acc. voltage (kV)		
		5	10	20
Si	Conv.	311	899	1415
	GE	68	122	171
Cu	Conv.	124	294	828
	GE	84	121	148
Au	Conv.	85	184	421
	GE	62	112	190

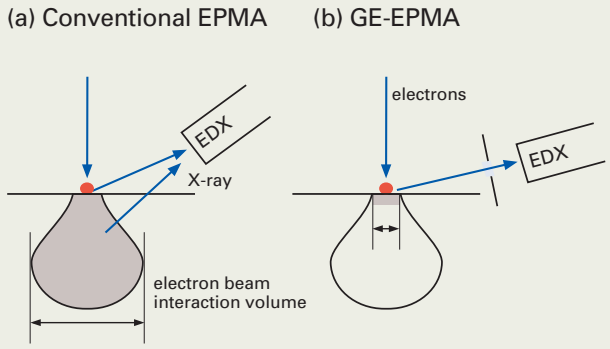

Fig. 1 Schematic of EPMA analysis by conventional EPMA and grazing-exit (GE) EPMA. The specimen is assumed to be a micro particle on a flat substrate.

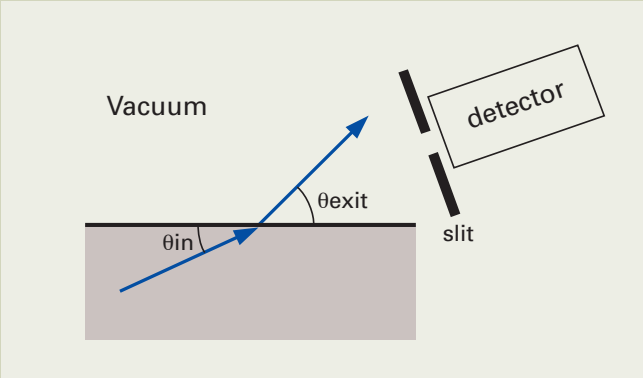

Fig. 2 Refraction effects of X-rays at the specimen surface.

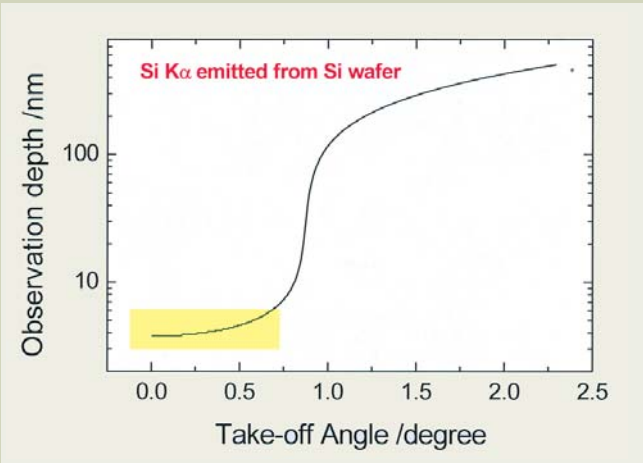

Fig. 3 Exit-angle dependence of analysis depth under grazing-exit conditions. This data is obtained by calculations of SiKα generated from a silicon wafer.

intensity. The reduction of this background enables one to perform micro-volume analysis and surface analysis. **Figure 5** shows the energy distribution of the continuous X-ray background from a silicon wafer at three different exit angles [9, 10]. Since the characteristic X-rays from Si are only observed at 1.74 keV and no characteristic X-rays appear in the energy region higher than this energy, the X-ray spectrum of Si is useful for measuring the continuous X-ray background. As indicated in **Fig. 5**, as the exit angle decreases, the continuous X-ray intensity also decreases. In particular, the decrease in continuous X-rays is noticeable in the low-energy region. This phenomenon seems to be related to the distribution of continuous X-ray generation in the depth direction; hence, it is possible to perform surface analysis at low exit angles (grazing-exit angles) with low background.

Thus, under grazing-exit conditions, the characteristic X-rays can be measured with high sensitivity even from the top surface of a thin film. For example, in the analysis of a Ti-Cr alloy film 4 nm thick formed on a Au film on a Si substrate, at an exit angle of 40°, the characteristic X-rays from Ti and Cr were not observed due to high continuous X-ray background; however, decreasing the exit angle resulted in clearly revealing Ti and Cr on the top surface due to the reduction of the background [11].

Improvement in lateral resolution in the specimen

As shown in **Fig. 1 (a)**, in conventional EPMA, even when a small electron probe with a diameter of 10 nm is used, the analysis region broadens due to the diffusion of electrons in the specimen. However, the broadening of the analysis region in the lateral direction is more noticeable in the deep regions than in the near-surface regions (although the difference in broadening is dependent on the specimen). That is, in the near-surface regions, the incident electrons do not broaden very much in the lateral direction.

This phenomenon can be estimated by Monte Carlo simulation of electron trajectories. A Monte Carlo simulation study was performed on the variation of the characteristic-X-ray generation region in the specimen with various accelerating voltages of the electron beam and constituent elements in the specimen. Especially, in order to evaluate the spatial resolution in the lateral direction for element analysis, the maximum diffusion width of the electron beam in the specimen was obtained under conventional EPMA conditions as shown in **Fig. 1 (a)**, then the diffusion width near the surface under the grazing-exit EPMA conditions (in **Fig. 1 (b)**) was estimated [12]. **Table 1** shows the estimated result. It was found that the grazing-exit EPMA drastically improves lateral resolution, more than ten times that with conventional EPMA. This improvement seems to be particularly noticeable for a matrix specimen of light elements. At present, an experimental study on the improvement in lateral resolution is in progress.

An application to the analysis of a micro particle specimen

It is well known that a trace amount of impurities on a semiconductor wafer greatly affects the performance of the semiconductor device. The increasing integration of semiconductor devices makes it necessary to address impurities at sizes smaller than a micrometer, requiring a method for analyzing such a micro particle. Other analysis methods such as Auger electron spectroscopy can be applied in some cases; however, the EPMA method is still effective considering the fact that it excels in quantification and that it can measure a particle of micrometer to sub-micrometer size.

However, as shown in **Fig. 1 (a)**, when the particle size becomes smaller, the electron beam can easily penetrate the particles and enter the wafer, generating high-intensity X-rays from the wafer. Therefore, if the particle contains the same element (Si, in a case of silicon wafer) present in the wafer, conventional EPMA measurement cannot distinguish between the Si X-rays that emerge from the

wafer and those from the micro particle. Moreover, as mentioned above, because the continuous X-ray background increases, it becomes difficult to analyze the trace elements in the micro particle. Consequently, we studied whether single-particle analysis is possible or not using the grazing-exit X-ray analysis method [13].

Figure 6 shows an X-ray spectrum obtained by an EDS measurement for a particle of Fe_2O_3 (particle diameter: about 1 μ m) on an Au thin film on a silicon wafer. **Figure 6 (a)** shows an X-ray spectrum measured under conventional EPMA conditions, namely a large take-off angle; the characteristic X-rays from the Au and Si under the micro particles appear with high intensities. On the other hand, **Fig. 6 (b)** shows an X-ray spectrum measured at a grazing-exit angle. The characteristic X-rays from Au and Si completely disappear, and only the characteristic X-rays from the Fe_2O_3 micro particles are observed. This shows that single-particle analysis is possible. Other than this analysis, there is a report on an application of the grazing-exit EPMA method to element analysis for an inclusion in a metal specimen [14]. This report shows that it is possible to analyze the inclusion by completely separating it from the matrix after exposing the inclusion in the metal specimen on the surface.

In addition, when this method is applied to a micro particle specimen, the electron beam should be set to the same size as the micro particle or smaller. This is because, if the electron beam size is larger than the particle as shown in **Fig. 7**, the characteristic X-rays generated from places other than the particle make it difficult to analyze the specimen. However, if the grazing-exit EPMA method is applied, restriction on the electron beam size gives no problems; because, even if the electron beam irradiates places other than the micro particle (for example, a substrate beneath the micro particle) and generates X-rays, the grazing-exit condition can prevent detection of these X-rays. **Figure 7** shows X-ray spectra measured under conventional EPMA conditions and grazing-exit conditions [11].

Summary

In the present article, we introduced the grazing-exit EPMA method and presented examples of applications that make use of its merit. On the other hand, a disadvantage of the grazing-exit EPMA method is that the charac-

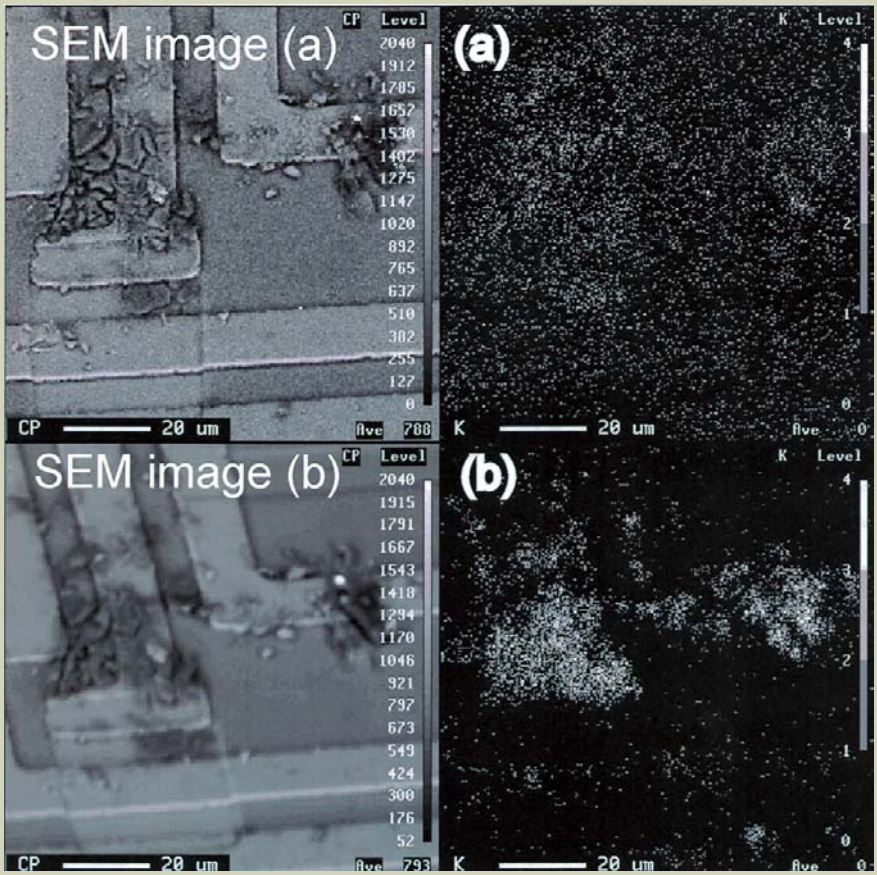

Fig. 4 Element mapping of K from contaminants on the specimen surface. (a) An element map obtained using conventional EPMA. (b) That obtained using grazing-exit EPMA.

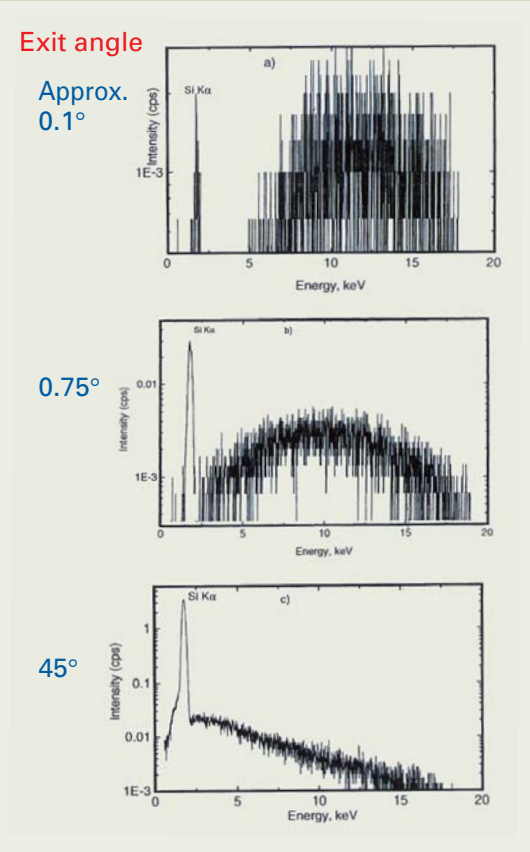

Fig. 5 X-ray spectra of a silicon wafer taken at various exit angles. The difference in energy distribution of the continuous X-ray background is clearly seen.

teristic X-ray intensity is weak. Of course, as mentioned above, the matters of importance are S/B ratio and surface sensitivity; it is wrong to state that the grazing-exit EPMA method has a disadvantage simply because its analysis-line intensity is weak. However, it is necessary to improve measurement efficiency; one method of doing so is to arrange multiple detectors around the specimen. Although the characteristic X-rays emerge in all directions, at present only a portion of them is measured. Therefore, it may be possible to drastically improve the measurement efficiency by using multiple detectors or a ring-shaped detector [2].

Furthermore, as the grazing-exit method has a connection with the total reflection X-ray fluorescence method, the specimen surface in principle must be flat. However, when the specimen consists of micro particles or has an uneven shape, one can also perform the EPMA measurement while keeping the advantages of the grazing-exit X-ray measurement as well as in the flat specimen. Consequently, the requirement of the grazing-exit method for the flatness of specimen is not as severe as that of the total reflection X-ray fluorescence method; from the practical point of view, this grazing-exit method may be applied to many kinds of specimens.

Acknowledgments

Part of this research was funded by a FY2003 Research Grant from the Kazato Research Foundation (Title of research: Application of Grazing-Exit X-ray Analysis to Commercial SEM-EDX (EPMA)) and the Grants-in-Aid for Scientific Research B2 (No. 12554030, Title of project: An Experimental Equipment for Grazing-exit Electron Probe X-ray Microanalysis and Analytical Results of Single Particle Such as Aerosol), from the Ministry of Education, Culture, Sports, Science and Technology of Japan. The author is grateful for their supports.

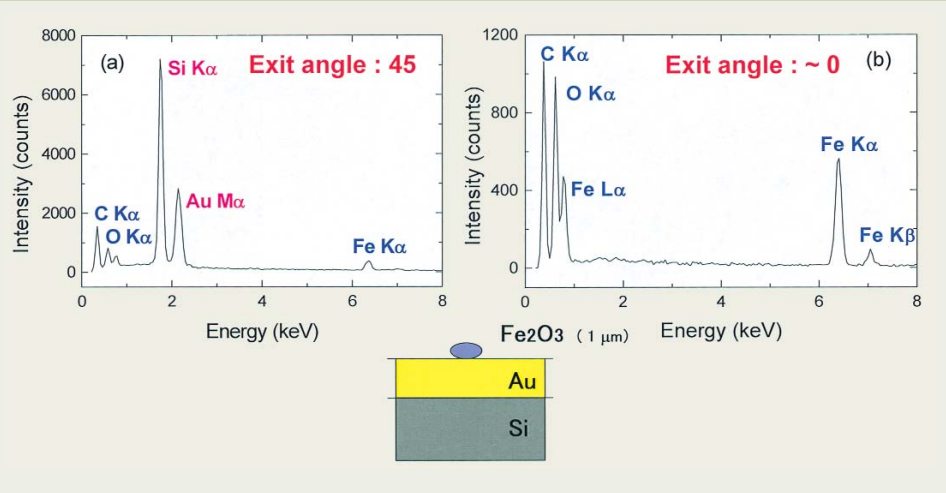

Fig. 6 Example of a single-particle analysis. The specimen is an Fe_2O_3 particle (size: about 1 μ m in diameter) captured on an Au thin film on a Si wafer. (a) X-ray spectrum measured at a take-off angle of 45°. (b) X-ray spectrum measured at an exit angle of nearly 0°.

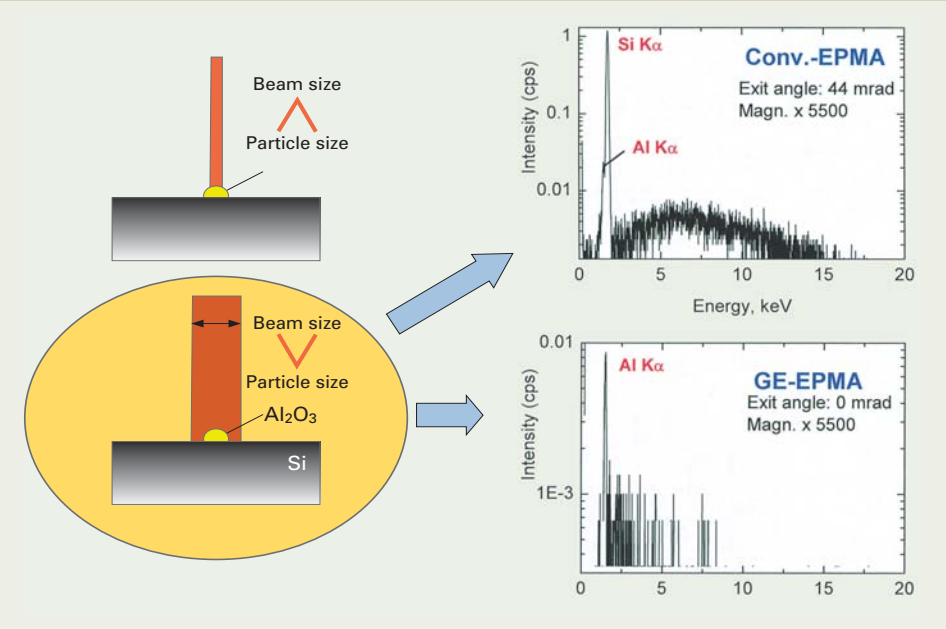

Fig. 7 Relationship between the electron beam size and particle size. An example of measurement is shown on the right when the electron beam size (actually, the region that electron beam scanned) is larger than the micro particle. An X-ray spectrum obtained at a take-off angle of 44 mrad is shown at the upper right. The spectrum shown at the lower right is measured at an exit angle of nearly 0°.

References

[1] K. Tsuji, Grazing-Exit X-Ray Spectrometry, X-Ray Spectrometry: Recent Technological Advances, edited by K. Tsuji, J. Injuk, and R. E. Van Grieken, John Wiley & Sons, Ltd, p. 293-305 (2004)

[2] K. Tsuji, Grazing-Exit X-ray Microanalysis – Its Applications to EPMA and XRF – *Bunseki*, **338**, 83-88 (2003) (in Japanese)

[3] K. Tsuji,Grazing-Exit Electron Probe X-ray Microanalysis in "Progress of X-ray Analysis", AGNE Gijutsu Center, Tokyo, **32**, 25-44 (2001) (in Japanese)

[4] K. Tsuji, Grazing-Exit Electron Probe X-ray Microanalysis – Its Applications to Surface Analysis and Micro-particle AnalysisAnalysis – *Materia*l, **39**, 586-593 (2000) (in Japanese)

[5] K. Tsuji, Z. Spolnik, and T. Ashino, New experimental equipment for grazing-exit electron probe microanalysis (GE-EPMA), *Rev. Sci. Instrum.*, **72**, 3933-3936 (2001)

[6] K. Tsuji, Y. Murakami, K. Wagatsuma, and G. Love, Surface Studies by Grazing-Exit Electron Probe Microanalysis (GE-EPMA), *X-Ray Spectrometry*, **30**, 123-126 (2001)

[7] T. Awane, T. Kimura, J. Suzuki, K, Nishida, N. Ishikawa, and S. Tanuma, *J. Surf. Anal.* **9**, 171 (2002)

[8] H. Takahashi, Inst. *Phys. Conf. Ser.*, **165**, 435 (2000) (Symposium 14, 2nd Conf. Int. Union Microbeam Analysis Societies, Kailua Kona, Hawaii, 9-13, July 2000)

[9] K. Tsuji, Z. Spolnik, and K. Wagatsuma, Continuous x-ray background in grazing-exit electron probe x-ray microanalysis, *Spectrochim. Acta B*, **56**, 2497-2504 (2001)

[10] Z. Spolnik, K. Tsuji, K. Saito, K. Asami, and K. Wagatsuma, Quantitative analysis of metallic ultra-thin films by grazing-exit electron probe x-ray microanalysis, *X-Ray Spectrometry*, **31**, 178-183 (2002)

[11] Z. Spolnik, J. Zhang, K. Wagastuma, and K. Tsuji, Grazing-exit electron probe x-ray microanalysis of ultra-thin films and single particles, *Anal. Chim. Acta*. **455**, 245-252 (2002)

[12] K. Tsuji, K. Tetsuoka, F. Delalieux, and S. Sato, Calculation of electron-induced x-ray intensities under grazing-exit conditions, *e-Journal of. Surface and Nanotechnology* **1**, 111-115 (2003)

[13] K. Tsuji, Z. Spolnik, K. Wagatsuma, R. Nullens, and R. Van Grieken, Detection limit of grazing-exit electron probe micro-analysis (GE-EPMA) for particles analysis, *Mikrochim. Acta*, **132**, 357-360 (2000)

[14] T. Awane, T. Kimura, K, Nishida, N, Ishikawa, S. Tanuma, and M. Nakamura, *Anal. Chem.* **75**, 3831-3836 (2003)

Fullerenes and Carbon Nanotubes: Nanocarbon Assuming a Leading Role in the 21st Century

Toshiya Okazaki[†] and Hisanori Shinohara[††]

Department of Chemistry/Institute for Advanced Research, Nagoya University

Introduction

Recently, the word "nanotechnology" is often seen and heard. As basic substances supporting nanotechnorogy, nanocarbon materials have been drawing much interest. In particular, fullerenes of a highly symmetric spherical molecule with a diameter of around 1 μm, and superfine carbon nanotubes (CNTs) with a diameter of 1 nm and length of several mm are considered, respectively, as prototypes of 0 and 1 dimensional nanomaterials due to their rare structures.

Moreover, applications of these novel materials to nanotechnology are already under development [1]. However, it is not an overstatement to say that research and development for these substances is still at the dawn. Recently, although C_{60} and C_{70} can be purchased at a considerably cheaper price (mixed fullerenes consisting of C_{60} and C_{70} is about 500 yen per gram), many other fullerenes are still expensive. Most all CNTs which can be purchased also contain many impurities, such as amorphous carbon and catalyst metal. A CNT sample with uniform diameter and length does not yet exist.

In the latest research, the discovery of new fullerenes and new CNTs is still a hot theme. In addition, for development of new methods of synthesis, in the separation or isolation of a substance, and the determination of structure or the evaluation of purity, many areas of improvement still exist, and much energy is being concentrated on these studies.

Since fullerenes and CNTs present an ongoing research challenge, it will be useful for people who are going to investigate using fullerenes and CNTs to know how to synthesize, separate and evaluate fullerenes and CNTs. This article explains fullerenes and CNTs, focusing on the common methods of synthesis and indispensable analytical techniques for these materials.

[†]He now works for Research Center for Nano-Carbon at National Institute of Advanced Industrial Science and Technology (AIST), Tsukuba Central-5 Higashi 1-1-1, Tsukuba Ibaragi, 305-8565, Japan
E-mail: toshi.okazaki@aist.go.jp
[††]Furo-cho, Chigusa-ku, Nagoya City, Aichi Prefecture, 464-8602
E-mail: noris@cc.nagoya-u.ac.jp

Fullerenes

Method of synthesizing fullerenes

Fullerenes can be synthesized using several methods in the laboratory. The main methods are the laser-vaporization method, the arc-discharge method, and the combustion method.

In all these methods, it is necessary for high-density vapor and plasma containing many carbons to be generated. Commonly, C_{60} (**Fig. 1 (a)**) and C_{70} are generated. The laser vaporization method was used in early fullerene synthesis. Although this method has high yield and is suitable for fundamental experiments, it is not suitable for the large-scale production of fullerenes.

So far, the most generally used synthesis method for the large-scale production of fullerene is the arc discharge method, which uses carbon electrodes in a rare gas under low pressure.

Actual optimum synthesis conditions, such as the size of the discharge chamber, change somewhat with each instrument. In our laboratory, the large-scale synthesis of fullerenes is performed using a larger carbon electrode (diameter of about 2 cm) than usual for the anode, and causing arc discharge with a direct current of 300-500 A between electrodes. Arc electric discharge takes place under a helium environment of 40-150 Torr. In arc electric discharge, the yield of fullerenes increases when helium is used. In order to cause stable arc electric discharge, the distance between the electrodes is held to 1 to 3 mm during electric discharge. At this time, the voltage between the two electrodes is about 20 V, and the temperature of the arc plasma near the cathode reaches around 4,000°C. When synthesizing endohedral metallofullerenes (fullerenes with metal atoms encapsulated), a rod made of carbon mixed with metal compounds (metal oxides) is used as an anode.

Recently, the combustion method has been attracting attention as a very useful method of synthesizing fullerenes in larger scale. The combustion method is the method of burning aromatic compounds, such as toluene, in argon gas under low pressure. Since materials are very cheap and allow for continuous synthesis, this is an industrially advantageous method.

Extraction and isolation of fullerenes

The synthesis methods introduced above generate a lot of soot in the chamber. Fullerenes are found in the soot. Since the highest yield of fullerenes is about 20%, fullerenes must be isolated efficiently from the soot. There are two different methods for extracting fullerenes from the soot.

The method usually used is Soxhlet's extraction using organic solvents, such as carbon disulfide and toluene. This method can remove soot and other materials that are insoluble in the organic solvent. However, soluble hydrocarbon impurities are also mixed with the solvent in the extraction liquid obtained. Moreover, fullerenes become very hard to dissolve with increasing molecular weight. For example, when toluene is used, extraction of C_{100} or larger fullerenes is very difficult.

Another method is the sublimation method. The soot generated is put into a quartz pipe, and the fullerene is sublimated by heating in a vacuum. The sublimated fullerene is trapped in a cooling portion. Although this method can be used for fullerenes which do not dissolve in an organic solvent, this method uses a high temperature (above 400°C) for sublimation, leading to a decomposition of many fullerenes. Thus, it cannot be considered that sublimation is an efficient extraction and separation method.

It is difficult for both methods discussed above to isolate a single size fullerene. Generally, to do that, high-performance liquid chromatography (HPLC) is used for separation and purification after extraction. At present, exclusive HPLC (high-performance liquid chromatography) columns are available just

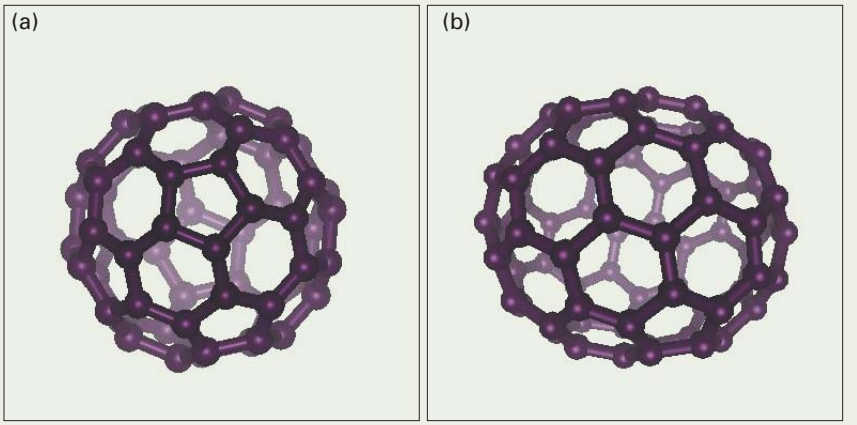

Fig. 1 Molecular structure of fullerenes. (a) $C_{60}(I_h)$ and (b) $C_{76}(D_2)$.

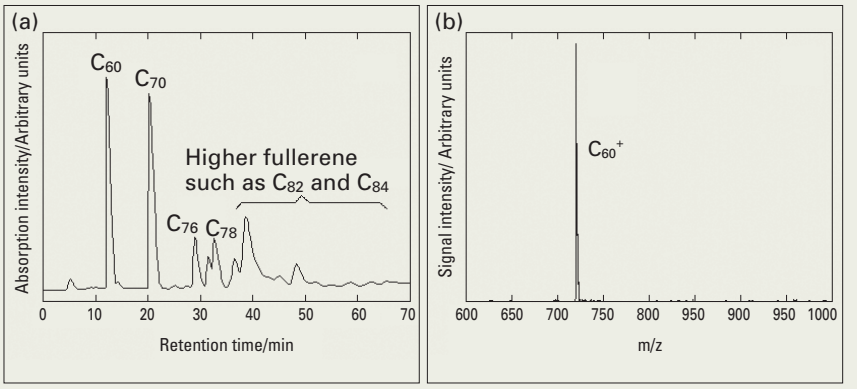

Fig. 2 (a) HPLC scheme of Soxhlet extracted solution (Column: Buckyprep (Nacalai Tesque)), Mobile phase: toluene, flow rate: 12 mL/min) (b) Positive ion mass spectrum of isolated C_{60}.

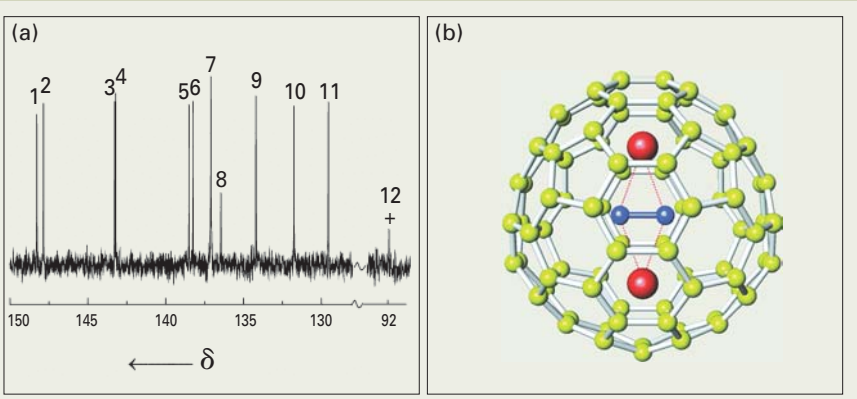

Fig. 3 Structure determination of endohedral metallofullerene $(Sc_2C_2)@C_{84}$ that encapsulates scandium carbide (Sc_2C_2). (a) ^{13}C NMR spectrum and (b) the corresponding molecular model [3].

for fullerene separation. The target fullerene can be isolated by combining different kinds of columns. For the bonding phase in the stationary phase of those columns, an aromatic ring compound, such as pyrenylethyl (PYE), pyrenylpropyl (PYP), or pentabromobenzyl (PBB) is used. **Figure 2 (a)** shows the chromatogram for Soxhlet extracted solution of soot generated by the arc-discharge method. When the C_{60} fraction is collected and its mass spectrum is measured (**Fig. 2 (b)**), it is shown that C_{60} is almost completely isolated. Recently, a trial of separation of two kinds of C_{76} (**Fig. 1 (b)**), dextrorotary and levorotary, has also been done using a column for separating optical isomers [2].

As discussed above, an isolated fullerene can be confirmed by measuring a mass spectrum, HPLC, and an absorption spectrum, and by comparing them with existing data. When using mass spectrometry, since the signal of a hollow fullerene may be emphasized in the negative-ion spectrum, and the signal of endohedral metalofullerene may be emphasized in the positive-ion spectrum, caution is required. If isolated fullerene is kept in solution in carbon disulfide, this fullerene is comparatively stable and can be stored over a long period of time.

Structure-determination methods

To determine the structure of fullerenes, nuclear magnetic resonance (NMR) is often used in the same way as in synthesis research for many organic compounds. However, since a fullerene does not have a proton in the molecule, structure analysis must be performed using ^{13}C-NMR. Because the natural abundance of ^{13}C is as low as 1.10%, in order to obtain a spectrum with a good S/N ratio, a high-concentration sample must be prepared. Therefore, NMR measurement for a very small amount of fullerenes is difficult. Moreover, since only the symmetry of a molecule is obtained as information from 1-D ^{13}C-NMR, structural isomers may not be distinguished.

As an example, the ^{13}C-NMR spectrum of the endohedral metallofullerene $(Sc_2C_2)@C_{84}$, encapsulated with scandium carbide (Sc_2C_2) (@ means encapsulation) is shown in **Fig. 3** [3]. In 12 of the ^{13}C-NMR signals, 11 are observed in the area (δ= 129.55 to 148.27 ppm) where carbon signals originate from an sp^2 hybrid orbital in the fullerene. One signal remains in the area (δ= 92 ppm) where a carbon signal derives from the sp hybrid orbital. Although $(Sc_2C_2)@C_{84}$ cannot be distinguished from $Sc_2@C_{86}$ by mass spectral analysis, a C_{86} cage which matches this NMR pattern does not exist. The pattern of the NMR spectrum actually observed in the sp^2 range of fullerene (10×8; 1×4) coincides with the pattern of D_2d-C_{84}. That is, the signal observed in the area of the sp hybrid orbital comes from scandium carbide (Sc_2C_2). It can be understood that this molecule is endohedral metallofullerene $(Sc_2C_2)@C_{84}$, encapsulated scandium carbide (Sc_2C_2).

Also using X-ray diffraction measurement, the structures of various fullerenes have been revealed. The analysis of the complicated molecular structure of a fullerene demonstrates the effectiveness of the maximum entropy method (MEM) [4]. First, analysis using the Rietveld method is performed using the molecule model which assumes a uniform charge

density of a spherical cell as a starting point, and then a structure factor is estimated from powder diffraction data. Then, imaging for electron charge density is created, on the basis of the result, by using MEM. The electron charge density map and molecular structure of $Sc_2@C_{66}$ determined by this technique are shown in **Fig. 4**. Although the fullerene molecule has a structure consisting of pentagons and hexagons, if the pentagons are close to each other, distortion of the cage will become large and the fullerene will not stabilize. This is called the isolated pentagon rule (IPR). All hollow fullerenes generated and isolated have so far satisfied this empirical rule.

However, a stable fullerene which violates the IPR can be generated by encapsulating metal atoms. $Sc_2@C_{66}$ shown in **Fig. 4** is the first fullerene which violated IPR. In this endohedral metallofullerene, two Sc atoms form an Sc_2 dimer, and they nestle with fused pentagons. Two electrons are transferred from the Sc_2 dimer to the C_{66} cage, and the electronic structure of the whole molecule becomes $(Sc_2)^{2+}@C_{66}^{2-}$. That is, the electron density of the pentagons increase, and the molecule is stabilized by electron transfer from Sc.

It is very interesting to observe whether the fullerene structure becomes large by holding its spherical shape or grows long and tubular in the shape of a nanotube, with the number of carbons and their size increasing. Huge C_{166} and C_{120} fullerene molecules have been isolated so far, and their shapes were observed using the scanning tunneling microscope (STM) [6, 7]. From the STM image, the spherical shape can be observed, and as a result, it can be recognized that a "basket-like" structure like that of C_{60} is kept.

There is also the structural-analysis method using the so-called peapod in which fullerene is encapsulated into a single-wall carbon nanotube (SWNT). When observing the peapod with a transmission electron microscope (TEM), the inside structure of the endofullerene molecule can be seen transparently. The positions of the Sc atoms in $Sc_2@C_{84}$ (I) were determined using TEM images [8]. Although the ^{13}C-NMR measurement of $Sc_2@C_{84}$ (isomer I) can be shown to have *C*s symmetry, two Sc atoms could be located anywhere on a plane of mirror symmetry, and their position cannot be clearly determined using only the ^{13}C NMR spectrum. The results of analysis using the image simulation show that two Sc atoms are in a position 0.20 nm from the center of a fullerene cage, and that the Sc-Sc distance is 0.35 nm.

The electronic structure of fullerene

The UV (ultraviolet), visible, or near infrared absorption-spectrum measurement of fullerene is one of the easiest and most powerful methods for identifying fullerene. Since the shape of the absorption spectrum reflecting the electronic structure depends greatly on the molecular structure of the fullerene or the valence, the symmetry of a molecule can be discussed by comparing it with the absorption spectrum of an already isolated fullerene.

In particular, in order to estimate the symmetry and electronic state of endohedral metallofullerene, shape comparison with an absorption spectrum is used. Generally, in endohedral metallofullerenes, intramolecular electron transfer takes place. Two or three electrons usually transfer from the outermost shell of the encapsulated metal to the fullerene cage. If the number of electrons that transfer and the symmetry of the fullerene cage are the same, since the absorption spectra of those endohedral metallofullerenes are very similar, comparison of absorption spectra becomes a powerful means to surmise the symmetry and electronic structure of endohedral metallofullerenes.

In order to obtain information on the electronic structure of fullerene, ultraviolet photoelectron spectroscopy (UPS), X-ray photoelectron spectroscopy (XPS), and electron energy-loss spectroscopy (EELS) are used as analytical tools. **Figure 5** is an EELS spectrum acquired from endohedral Sm fullerenes composed of C_{74} to C_{84} [9]. In this energy range, the M absorption edge (M_4 and M_5) of the Sm atom can be observed. The peak position is very sensitive to the number of valence electrons of Sm. Compared with the bottom spectrum of Sm_2O_3 which is the Sm^{3+} reference substance, all the signals from endohedral Sm fullerenes have shifted to lower energy. This shows that the valence of Sm is +2 in all these fullerene cages, and independent of the size of the cage. Consequently, it is concluded that the electronic structure of all the molecules is $Sm^{2+}@C_{2n}^{2-}$ (2n= 74, 78, 80, 82, 84).

Physical properties of fullerenes and examples of their applications

Concerning the physical properties and applications of fullerenes, various attractive characteristics have already been discovered. This section introduces two typical examples.

Fullerenes build molecular crystals as if they were atoms. In solid C_{60}, the h_u band originating in 5-fold-degenerated HOMO creates the conduction band, and the t_{1u} band originating in 3-fold-degenerated LUMO creates the valence band. The C_{60} solid shows superconductivity when doped with an electron in a degenerated t_{1u} band. The transition to superconductivity was first discovered in the K_3C_{60} crystal potassium doped C_{60}. The transition temperature is 18 K. This discovery was the underlying cause of the fullerene fever in the 1990s.

By adding a hydrophilic group to fullerenes, water-soluble fullerenes can be synthesized. Although fullerenes are generally soluble in organic solvents, since they do not dissolve in water, processing to make them dissolve in water is necessary for biological applications. For example, there is an application in MRI (magnetic resonance imaging) using $Gd@C_{82}(OH)_n$ which adds the hydroxyl group to $Gd@C_{82}$ as a contrast media (contrast reagent). In animal experiments using rats or mice, it shows a contrast capability (i.e., relaxivity) 20 times larger than those of commercially available ones [10].

Carbon Nanotubes

Methods of carbon nanotube synthesis

● Arc-discharge method

Two kinds of carbon nanotubes with perfect structures, SWNT (single-wall carbon nanotubes) and MWNT (multi-wall carbon nanotubes), exist. SWNT has a structure in which one graphitic sheet is wrapped up to form a seamless cylinder (**Fig. 6**). The shape of a MWNT is like nested SWNTs.

The first CNT discovered was a MWNT. During the synthesizing of fullerenes using the direct-current arc-discharge method, slag-like sediment was generated on the top of the cathode. From the smooth black powder which is near the center of this sediment, an MWNT whose diameter was several tens of nanometers was discovered. MWNTs do not exist in the soot in the chamber. The yield of MWNT reaches a maximum when discharging at pressures about 500 Torr higher than the pressure at which fullerene is best generated. However, when the current is too high and the chamber reaches a high temperature, since graphite will be generated in preference to MWNT, the yield of MWNT decreases.

Similarly, SWNT can be synthesized using the arc-discharge method. In this case, in order to change from the conditions for synthesizing MWNT, a carbon electrode with a metal compound added must be used as an anode. This metal plays the role of a catalyst which stimulates the growth of the SWNT. The metal catalysts generally used are Fe, Co, and Ni or combination of two of these. Moreover, rare earth metals, such as La and Y, also have a catalytic effect in SWNT synthesis. The greatest yield of SWNT is obtained when Ni/Y or Ni/Fe binary element catalyst systems are used.

If this composite rod is evaporated by the arc-discharge method, cotton-like soot containing SWNT will accumulate in the chamber. The optimal pressure at the time of SWNT generation like that for MWNT is a comparatively high pressure of about 500 Torr. The length and diameter of the SWNTs generated depend on the kind of metal catalyst used, and the temperature at the time of generation. The diameter of the SWNTs is usually 1-3 nm.

Double-wall carbon nanotubes (DWNT), which is situated midway between a single-wall and a multi-wall, can be synthesized selectively. When synthesizing DWNTs using the arc-discharge method, composite carbon, to which sulfur is added as a sub-catalyst to three metals catalysts (Fe, Ni, and Co), is used [11]. In this case, the mean diameter of the DWNT generated is 3 to 4 nm. Moreover, it was shown recently that a thin DWNT with a diameter of 2 nm or less can also be synthesized by a pulsed arc discharge (with a pulse duration of up to 600 μs) [12]. By performing high-temperature heat treatment, the yield of this DWNT can be increased up to 90%.

● Laser-vaporization (furnace) method

Also in the laser-vaporization method, SWNTs can be synthesized using metal composite graphite.

Board-like metal composite carbon is installed in the central part of a quartz pipe inserted in a tubular electric furnace. There it is irradiated with a high power pulse laser (usually with 532 nm light, the second harmonic of a Nd: YAG laser), causing laser vaporization. The scattered carbon clusters are passed through the electric furnace downstream in the flow of a buffer gas, such as Ar, and SWNTs are synthesized due to the metal catalyst effect in the gas phase. Typical condi-

tions for synthesis include a pressure of 500-700 Torr and a temperature of around 1,200°C in the electric furnace. The diameter distribution of synthesized SWNTs is narrow as compared with other synthesis methods, and the distribution can be controlled to some extent by the ambient temperature [13]. In general, SWNTs obtained by this method have higher purity than SWNTs synthesized by the arc-discharge method.

Chemical vapor deposition (CVD) method

The Chemical Vapor Deposition (CVD) method can synthesize a large amount of MWNT, with almost no impurities, at a low temperature (1,000°C or less) and at comparatively low cost.

For example, catalysts, such as Co-Fe, are coated on a support material, such as zeolite, and mixture of acetylene and nitrogen flows over it (CCVD method). Generally, the MWNTs created by the CVD method have many surface defects compared with MWNTs generated by other methods.

However, the graphite phase can be crystallized well by processing the synthesized MWNT at a high temperature of above 2,000°C under an environment of inactive-gas, such as nitrogen. This CVD method is now the main method of synthesis for MWNTs. Several companies in Japan and other countries are preparing to mass-produce MWNT using this method. In addition, it is shown that DWNTs can also be synthesized selectively using the CCVD method with a proper zeolite support material [14].

SWNTs can also be synthesized using the CVD method, using carbon monoxide as a source of carbon (high-pressure carbon monoxide method, HiPco method).

SWNTs synthesized by the HiPco method have the following general features:

- There are few carbon impurities other than nanotubes.
- The diameter is comparatively thin, 0.8 to 1.3 nm, and the diameter distribution is large compared with SWNTs synthesized by the laser vaporization method.
- The surface has many defects like MWNTs.

SWNT synthesized using this HiPco method is sold for about $500/g by a U.S. company called Carbon Nanotechnology (CNI).

Furthermore, it was recently reported that SWNTs of high purity could be synthesized using the CCVD method employing alcohol as a source of carbon [15]. Because high-purity SWNT may be obtained by this method, it is considered that impurities, such as amorphous carbon, can be removed effectively using the etching effect of OH radicals generated during synthesis. In particular, when methanol is used, there is the feature that SWNT can be also synthesized at a temperature as low as 550°C conventionally.

Purification and quality evaluation

Regardless of the method used now, it is very difficult to synthesize CNTs with a yield of 100%.

Therefore, it is necessary to purify CNTs after synthesis. Fullerenes can dissolve in an organic solvent, so chemical purification methods, such as HPLC, can be applied for purification, and they can be purified to 99% or more. However, since the molecular weights of CNTs are large, and they are insoluble in solvents, it is difficult to purify CNTs using the same method as fullerenes. In this case, impurities, such as amorphous carbon and catalyst metal, can be removed by boiling (heating) soot containing CNTs in hydrogen peroxide water, hydrochloric acid or nitric acid [16-18].

What kind of purification method is used differs greatly with the kinds and purity of syn-

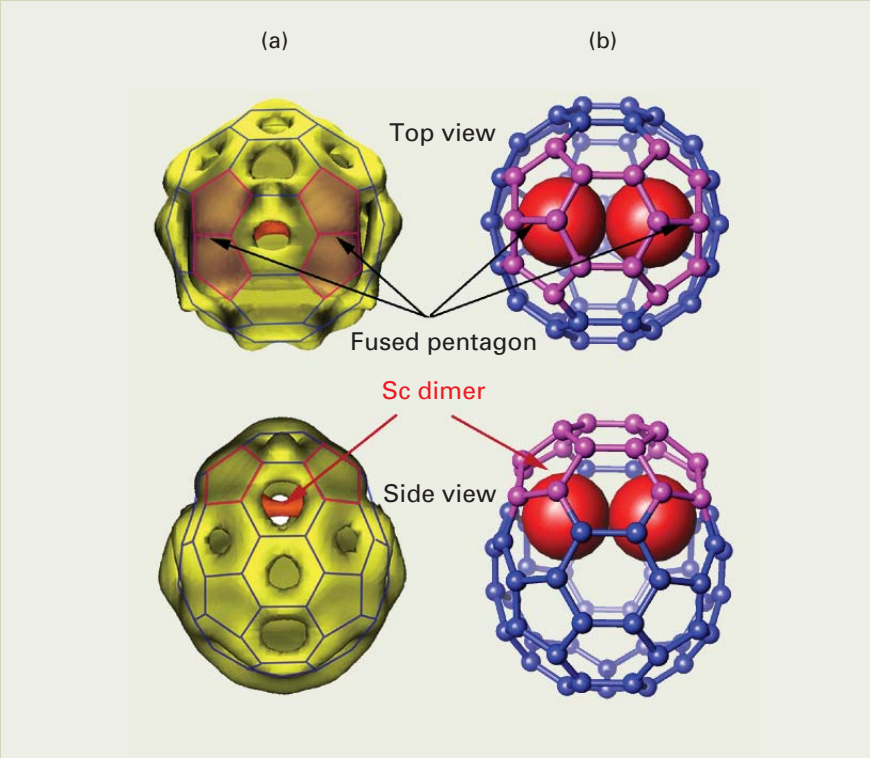

Fig. 4 Structures of $Sc_2@C_{66}$ first violating IPR. (a) Electron charge density map obtained by X-ray diffraction with MEM and (b) molecular structure [5].

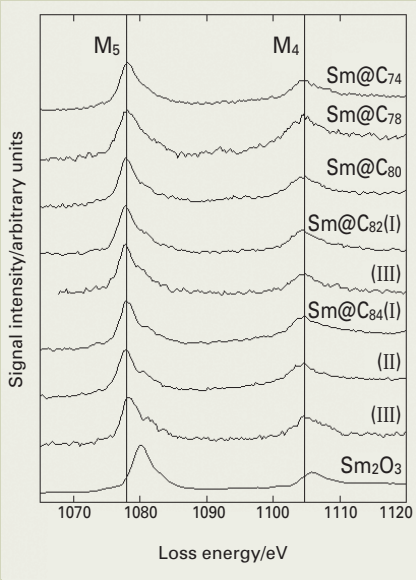

Fig. 5 EELS spectra of $Sm@C_{2n}$ ($74 \leq 2n \leq 84$). Bottom EELS spectrum of Sm_2O_3 is used for a reference of Sm^{3+} [9].

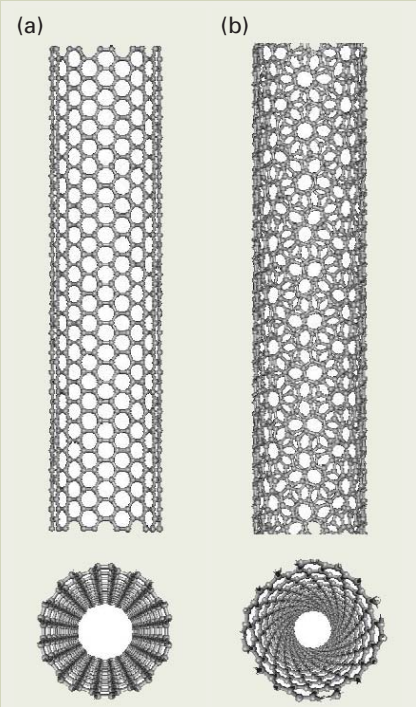

Fig. 6 Structures of (a) metallic SWNT and (b) semiconductor SWNT. Their chiral indexes are (10,10) and (15, 4), respectively.

thesized CNT. Furthermore, when graphite substances exist as impurities, since graphite is more stable than CNT, it is difficult to remove. Therefore, it is important to synthesize CNT without generating such impurities from the beginning.

In order to evaluate the quality of CNTs, shape observation using an electron microscope is indispensable. **Figure 7 (a)** is the SEM (scanning electron microscope) image of a SWNT synthesized by the CVD (HFCVD) method using a thermionic-emission filament [19]. It is found that a bunch of SWNTs extends in the shape of a cobweb on a zeolite particle of 400 to 500 nm. Since the SEM captures the shape of the surface of a sample, it is difficult to distinguish between the SWNT bundle and thin layer MWNTs, such as DWNTs. Moreover, with the ordinary SEM resolution, it is difficult to observe the SWNTs one by one (up to 1 nm) and fine amorphous carbon.

For these materials, shape observation is then usually performed by TEM. **Figure 7 (b)** is a TEM image of the same SWNT. Surely, it is found that SWNTs with few defects on the surface are synthesized with high purity and high yield. However, in observations using electron microscopes, especially by TEM, images show only part of a sample; therefore, these observations are not suitable for quantitative discussion.

Evaluation by resonance Raman scattering is performed in the quantitative discussion of the purity of CNT, or its molecular structure. The resonance Raman spectrum obtained from SWNT described above is shown in **Fig. 8**. Since the D-band of 1,370 cm^{-1} arising from amorphous carbon is much weaker than the G-band of 1,590 cm^{-1} arising from in-plane vibration of graphite, it is found that the purity of SWNT synthesized by this method is high. The band that appears near 1,550 cm^{-1} is a Breit-Wigner-Fano (BWF) band originating in metallic SWNT. Moreover, the so-called radial breezing mode (RBM) which appears around 100 to 300 cm^{-1} is also a characteristic signal of SWNT. It is known that there is an inverse proportionality in RBM to the diameter of the SWNT. The frequency of the RBM can allow for estimates of the diameter of synthesized SWNT. In the case of this sample, a diameter is 0.8 to 1.5 nm.

However, there is also a problem in this method. The electronic state density of CNT diverges at a certain energy by van Hove singularity, which is a feature of low-dimensional substance. Therefore, the absorption intensity of CNT between these singularities is extremely strong. So, if the excitation wavelength is varied for the same sample, the Raman signal with a different resonance frequency from CNT is also captured selectively, and the Raman spectrum shows a different feature. That is, although quantitative analysis can be performed by Raman spectroscopy for CNT which can be excited by a certain excitation wavelength, since CNT is usually a mixture of compounds having various structures (unless Raman observation using various laser wavelengths is carried out) no exact evaluation of the whole sample can be achieved.

In addition, in the quantitation of synthesis yield for CNT, or a residual metal catalyst, thermogravimetric analysis (TGA) is frequently used. Usually, CNT burns at 500 to 800°C in air. On the other hand, amorphous carbon burns at 500°C or less, and the metal catalyst cannot burn completely, and it remains at 800°C or more. Therefore, CNT can be distinguished from the amorphous carbon and the metal catalyst, and quantitative analysis can be performed.

Structure-determination methods

CNT has a structure composed by folding a graphene sheet into the shape of a tube. CNT becomes a metal or semiconductor depending on the way of this folding.

The molecular structure of SWNT is uniquely defined by two integers called the chiral indexes (*n*, *m*). For example, in **Fig. 9**, suppose that a nanotube is made so that the points shown by origin O and (6, 2) overlap. Since the positional vector of this point can be expressed as **6a+2b** using the two lattice vectors **a** and **b**, the chiral indexes of this nanotube become (6, 2). The SWNT is a metal if the difference in the chiral indexes is a multiple of 3 (**Fig. 6 (a)**). It becomes a semiconductor if difference in the chiral indexes is not a multiple of 3 (**Fig. 6 (b)**). On the other hand, the electronic property of MWNT can be interpreted as a linear combination of that of SWNT because the interaction between layers in MWNT is very weak.

The chiral indexes can be obtained by analyzing the electron diffraction pattern obtained from every CNT. Actually, the structure of CNT was clarified for the first time by this method [20]. This method enables one to measure the chiral index of each layer constituting CNT independently, for not only SWNT but also MWNT.

In addition, the chiral indexes can also be determined from the surface observation of SWNT by STM. When using the STM technique, the diameter of SWNT and the angle between the direction which a graphene sheet folds and its tube axis, called the chiral angle, are first determined from the STM image. These two parameters are uniquely related to the chiral indexes, and one can calculate the indexes from those values.

Furthermore, the chiral indexes can also be identified from the diameter estimated from the RBM described above and its resonance wavelength by the Raman spectrum; hence its structure can be determined [21].

Example of application of carbon nanotubes

The leading application of CNTs at present is a field-emission source.

The field emission is created when the electrons in the metal are thrown out by the tunneling effect in a vacuum generated by applying a high voltage to a fine tip. In order to cause

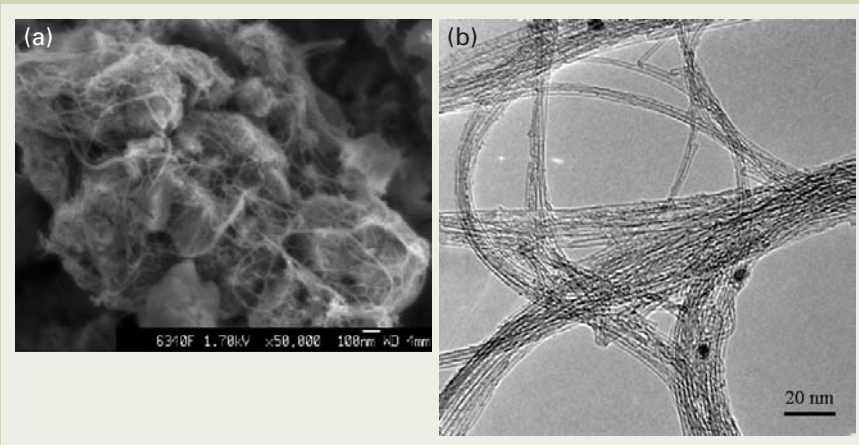

Fig. 7 Images of SWNT synthesized by the HFCVD method. (a) SEM image and (b) TEM image [19].

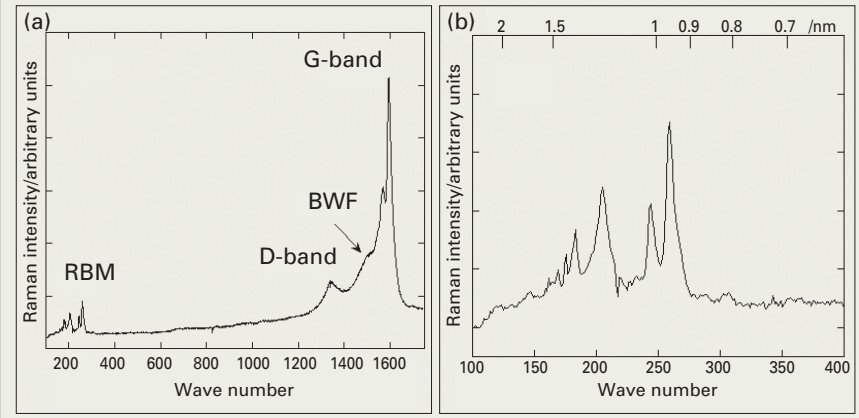

Fig. 8 (a) Raman spectrum of SWNT synthesized by the HFCVD method, and (b) expanded view of its spectrum in the low wavelength range. Excitation wavelength is 488 nm [19].

field emission, it is necessary to apply a strong electric field exceeding 10^7 V/cm to a metal surface. For producing such a strong electric field, a metal tip with a finely sharpened apex has been usually used.

However, since a CNT has a radius of curvature of the order of 1 nm, and it is chemically and physically tough, CNT attracted attention from early on as an ideal source of field emission to replace metal tips. A flat panel display using MWNT as a field-emission source is already being developed by Samsung SDI of Korea and Noritake Company of Japan, and its utilization lies in the near future. When using a conventional field-emission source, a current density of 10 mA/cm^2 is required to illuminate a panel; however, when MWNT is used, the current density reaches 0.1 to 1 A/cm^2 and the display operates stably for 20,000 hours or more.

These CNT displays have the advantages of low power consumption, high luminosity, wide field of view, fast response, and large area. Moreover, a super fine CNT of 1 nm diameter, which becomes a semiconductor and metal, attracts great attention as the nano-electronic material to replace silicon. One of the advantages of applying CNT to electronics will be that CNT allows the creation of devices with various electron transport characteristics using its different molecular structures. For example, experiments have shown that SWNTs in which a metal nanotube and a semiconductor nanotube are connected in one line becomes a diode. In addition, the electronic properties of CNT can be controlled by doping an ion to a SWNT from outside, or by doping a fullerene in the space within a SWNT [22]. Also a logic circuit has already been made using a CNT-FET (field effect transistor). IBM researchers created a NOT circuit, which is a basic computer circuit, using two SWNT-FETs having p-type and n-type characteristics [23].

Conclusion

The potential for application and utilization of fullerenes and CNTs is very high. In addition to the applications discussed so far, many studies are actively being carried out. Fullerenes have useful physical properties such as ferromagnetism and anti-cancer effects, and also it may be used as a model molecule for artificial photosynthesis by using its characteristics as an electronic receptor. Whereas CNT can be applied in various fields, such as the tip of a SPM (scanning probe microscope), hydrogen storage, artificial muscles, high-capacitance capacitors, secondary lithium ion batteries, and polymer composite materials. Certainly, the science of fullerenes and CNTs will increase and spread in future.

Finally, we introduce reviews of fullerenes and CNTs [24]. Since they explain the details of the matters discussed in this article, and various applications not written about here, please refer to them.

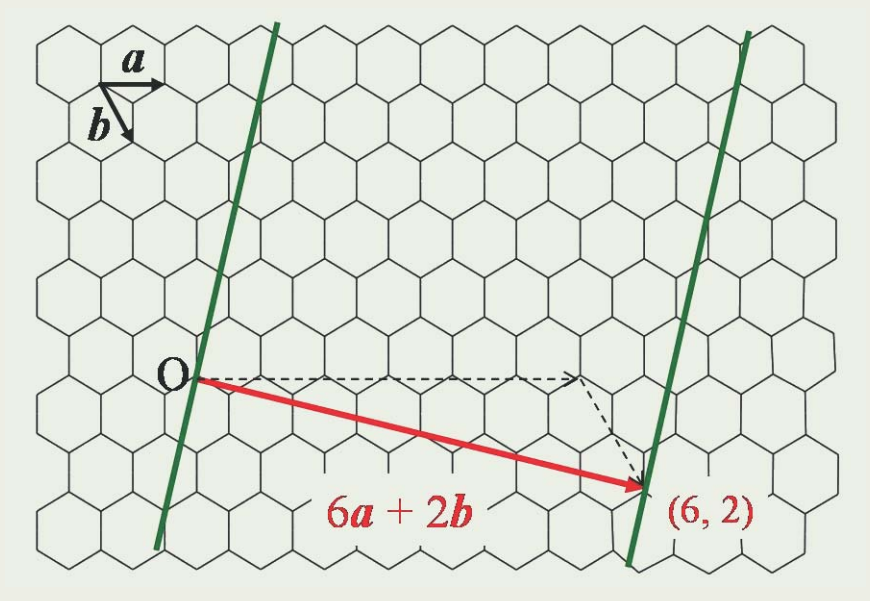

Fig. 9 Chiral indexes of CNT. a and b are basic translation vectors for a 2 dimensional hexagonal lattice.

References

[1] Nanotechnology — Developed into here — in Nikkei Science Separate Volume, **138**, Nikkei Science, Tokyo (2002) (in Japanese)

[2] C. Yamamoto *et al.*, *Chem. Comm*., **925** (2001)

[3] C. -R. Wang *et al.*, *Angew. Chem. Int. Ed*., **40**, 397 (2001)

[4] M. Takata, E. Nishibori, M. Sakata and H. Shinohara, New Diamond and Frontier Carbon Technology, **12**, 271 (2002)

[5] C. -R. Wang *et al.*, *Nature*, **408**, 426 (2000)

[6] Y. Achiba, *kagaku to Kougyou*, 52, 951 (1999) (in Japanese)

[7] K. Okada, A. Taninaka, T. Iwano, T. Sugai and H. Shinohara, Abstracts of the 19th Fullerene General Symposium, 30 (2000)

[8] K. Suenaga *et al.*, *Phys. Rev. Lett.*, **90**, 055506 (2003)

[9] T. Okazaki, K. Suenaga, Y. Lian, Z. Gu and H. Shinohara, *J. Chem. Phys*. **113**, 9593 (2000)

[10] M. Mikawa *et al*, *Bioconjugate Chem.*, **12**, 510 (2001)

[11] Y. Saito, Forefront of Nanomaterials, Chap. 16, Carbon nanotube, Kagaku-Dojin Publishing, Kyoto (2002) (in Japanese)

[12] T. Sugai *et al.*, *Nano Lett*., **3**, 769 (2003)

[13] H. Kataura *et al.*, *Carbon*, **38**, 1691 (2000)

[14] T. Hiraoka *et al.*, *Chem. Phys. Lett*., submitted

[15] S. Maruyama, R. Kojima, Y. Miyauchi, S. Chiashi and M. Kohno, *Chem. Phys. Lett.*, **360**, 229 (2002)

[16] A. G. Rinzler *et al.*, *Appl. Phys*. **A67**, 29 (1998)

[17] R. Rosen *et al.*, *Appl. Phys. Lett.*, **76**, 1668 (2000)

[18] I. W. Chiang *et al.*, *J. Phys. Chem*. **B105**, 8297 (2001)

[19] T. Okazaki and H. Shinohara, *Chem. Phys. Lett*., **376**, 606 (2003)

[20] S. Iijima, *Nature*, **354**, 56 (1991)

[21] A. Jorio *et al.*, *Phys. Rev. Lett*., **86**, 1118 (2001)

[22] T. Shimada *et al.*, *Appl. Phys. Lett*., **81**, 4067 (2002).

[23] V. Derycke, R. Martel, J. Appenzeller and Ph. Avouris, *Nano Lett*., **1**, 453 (2001).

[24] For example,
(a) M. S. Dresselhaus, G. Dresselhaus and P. C. Eklund, Science of Fullerenes and Carbon Nanotubes, Academic Press, New York (1996),
(b) R. Saito, G. Dresselhaus and M. S. Dresselhaus, Physical Properties of Carbon Nanotubes, Imperial College Press, London (1998),
(c) K. M. Kadish, R. S. Ruoff (Ed.) Fullerenes, John Wiley & Sons, New York (2000),
(d) M. S. Dresselhaus, G. Dresselhaus, Ph. Avouris (Ed.), Carbon Nanotubes, Spring-Verlag, Berlin (2001)

Introduction of Products

Electron Beam Lithography System
JBX-3030MV

The JBX-3030MV is an electron beam lithography system for mask/reticle fabrication that meets the design rule of 90 to 65 nm. This system features pattern writing with high speed, high accuracy and high reliability, achieved by high-end technologies.

- Accelerating voltage: 50 kV
- Electron gun emitter: LaB_6 single crystal
- Beam shape: rectangle (variable shaped)
- Workpiece dimension: up to 178 mm square
- Field stitching accuracy: ±9 nm
- Overlay accuracy: ±12 nm

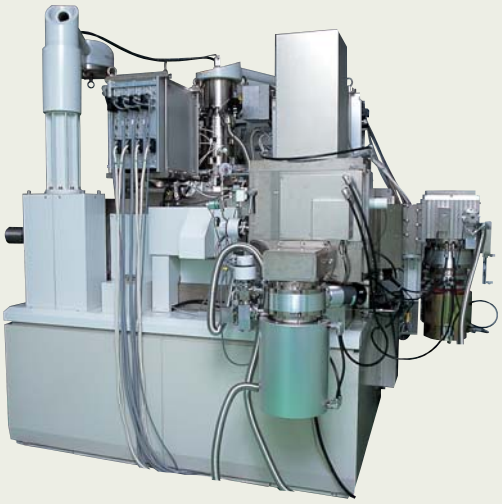

Electron Beam Lithography System
JBX-9300FS

Developed to meet nanometric lithography for next-generation devices. It employs a TFE gun and uses an ultra-high current density of 4000 A/cm^2. As advanced equipment in the increasingly refined lithographic technology, this high-precision, high-speed system is contributing to research and development.

- Accelerating voltage: 100 kV/50 kV
- Electron gun emitter: ZrO/W (Schottky)
- Beam shape: spot
- Minimum beam diameter: 4 nm (100 kV)
  7 nm (50 kV)
- Workpiece dimension: up to 300 mm in diameter

Electron Beam Lithography System
JBX-6000FS/E

The JBX-6000FS/E, which uses a 2000 A/cm^2 ultra-high current density TFE gun, was developed to meet the market's needs for nanometric lithography and production of FET devices, along with the advances in technology. As advanced equipment in the increasingly refined lithographic technology, this high-precision, high-speed system is contributing to research and development.

- Accelerating voltage: 50 kV/25 kV
- Electron gun emitter: ZrO/W (Schottky)
- Beam shape: spot
- Minimum beam diameter: 5 nm (50 kV)
  8 nm (25 kV)
- Workpiece dimension: up to 200 mm in diameter

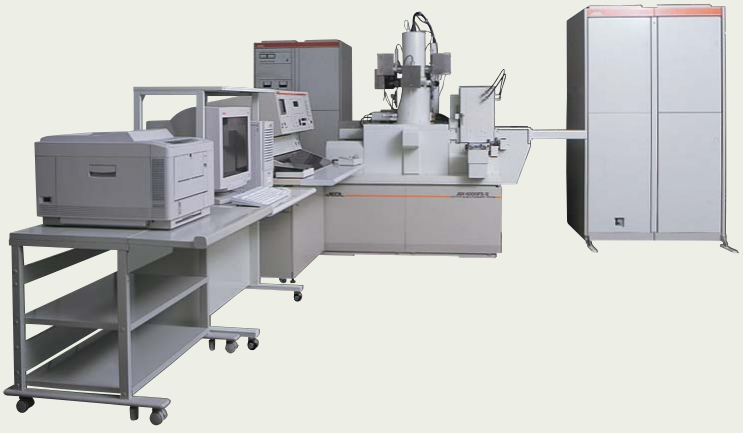

Introduction of Products

Ultra-Zoom Defect Review Tool

JWS-3000

The JWS-3000 is a high-resolution defect review SEM for 300 mm wafers. It achieves ultra-high resolution with ultra-low accelerating voltage to reduce irradiation damage on specimens such as low-k materials.

- Resolution: 3 nm at 1kV
- Accelerating voltage: 0.1 to 20 kV
- Wafer size: 300 mm & 200 mm
- Options: ADR/ADC, EDS, etc.

High Resolution Automatic Review SEM & FIB

JFS-9200/9300

The JFS series defect-review SEM/FIB system is a multi-function analysis tool for inline analysis and evaluation of semiconductor devices, with the catchphrase “Cut, See, and examine.” The JFS not only analyzes defects and failures beneath thin films but also evaluates structures of contact holes, which optical defect-review equipment and conventional SEMs cannot fully investigate.
The columns of an FIB and a SEM are positioned in such a way that the FIB mills and the SEM images the same points. (The angle between the ion gun of the FIB and the electron gun of the SEM is 60°). You can observe a high-resolution SEM image of a milled cross-section, without moving the stage.

Defect Review SEM

JWS-2000

The JWS-2000 is a wafer inspection system that provides necessary information for yield management in various semiconductor manufacturing processes. This fully automated SEM enables you to obtain high-resolution, high-tilt SEM images with high speed and high accuracy.

- Resolution: 5 nm (tilt angle: –15 to 60°, at 1 kV)
- Accelerating voltage: 0.5 to 15 kV
- Wafer size: 150 mm to 200 mm
- Options: ADR/ADC, EDS, CD measurement, etc.

JEOL Ltd. 1-2 Musashino 3-chome Akishima Tokyo 196-8558 Japan Sales Division ☎(042)528-3381 FAX(042)528-3386

http://www.jeol.co.jp/

ARGENTINA
COASIN S. A. C. I. yF.
Virrey del Pino 4071,
1430 Buenos Aires, Argentina
Telephone: 54-11-4552-3185
Facsimile: 54-11-4555-3321

AUSTRALIA & NEW ZEALAND
JEOL (AUSTRALASIA) Pty. Ltd.
Unit 9, 750-752 Pittwater Road,
Brookvale, N. S. W. 2100, Australia
Telephone: 61-2-9905-8255
Facsimile: 61-2-9905-8286

AUSTRIA
LABCO GmbH
Dr.-Tritremmel-Gasse 8,
A-3013 Pressbaum, Austria
Telephone: 43-2233-53838
Facsimile: 43-2233-53176

BANGLADESH
A.Q. CHOWDHURY & CO. Pvt. Ltd.
Baridhara Central Plaza 87, Suhrawardy Avenue
2nd Floor Baridhara,
Dhaka-12129 Bangradesh
Telephone: 880-2-9862272, 9894583
Facsimile: 880-2-988070

BELGIUM
JEOL (EUROPE) B. V.
Zaventem/Ikaros Business Park,
Ikaroslaan 7A, B-1930 Zaventem, Belgium
Telephone: 32-2-720-0560
Facsimile: 32-2-720-6134

BRAZIL
FUGIWARA ENTERPRISES
INSTRUMENTOS CIENTIFICOS LTDA.
Avenida Itaberaba,3563
02739-000 Sao Paulo, SPl Brazil
Telephone: 55-11-3983-8144
Facsimile: 55-11-3983-8140

CANADA
JEOL CANADA, INC.
(Represented by Soquelec, Ltd.)
5757 Cavendish Boulevard, Suite 540,
Montreal, Quebec H4W 2W8, Canada
Telephone: 1-514-482-6427
Facsimile: 1-514-482-1929

CHILE
TECSIS LTDA.
Avenida Holanda 1248,
Casilla 50/9 Correo 9, Providencia, Santiago, Chile
Telephone: 56-2-205-1313
Facsimile: 56-2-225-0759

CHINA
JEOL LTD., BEIJING OFFICE
Room No. B2101/2106,
Vantone New World Plaza,
No. 2 Fuwai Street, Xicheng District,
Beijing 100037, P. R. China
Telephone: 86-10-6804-6321/6322/6323
Facsimile: 86-10-6804-6324

JEOL LTD., SHANGHAI OFFICE
Sanhe Building 11F2, Yan Ping Road,
No. 121,Shanghai 200042, P.R. China
Telephone: 86-21-6246-2353
Facsimile: 86-21-6246-2836

JEOL LTD., GUANG ZHOU OFFICE
S2204 World Trade Center Building
371-375, Huang Shi East-Road, Guang Zhou,
510095, P. R. China
Telephone: 86-20-8778-7848
Facsimile: 86-20-8778-4268

JEOL LTD., WUHAN OFFICE
Room. 3216, World Trading Bld., 686 Jiefang Street,
Hankou, Wuhan, P. R. China
Telephone: 86-27-8544-8953
Facsimile: 86-27-8544-8695

FARMING LTD.
Unit 1009, 10/F., MLC Millennia Plaza
663 King's Road, North Point, Hong Kong
Telephone: 852-2815-7299
Facsimile: 852-2581-4635

CYPRUS
MESLO LTD.
Scientific & Laboraty Division,
P. O. Box 27709, Nicosia Cyprus
Telephone: 357-2-666070
Facsimile: 357-2-660355

EGYPT
JEOL SERVICE BUREAU
3rd Fl. Nile Center Bldg.,
Nawal Street, Dokki, (Cairo), Egypt
Telephone: 20-2-335-7220
Facsimile: 20-2-338-4186

FRANCE
JEOL (EUROPE) S. A.
Espace Claude Monet,
1, Allee de Giverny 78290
Croissy-sur-Seine, France
Telephone: 33-13015-3737
Facsimile: 33-13015-3747

GERMANY
JEOL(GERMANY)GmbH
Oskar-Von-Miller-Strasse 1,
85386 Eching Germany
Telephone: 49-8165-77346
Facsimile: 49-8165-77512

GREAT BRITAIN & IRELAND
JEOL (U.K.) LTD.
JEOL House, Silver Court, Watchmead,
Welwyn, Garden City, Herts AL7 1LT., England
Telephone: 44-1707-377117
Facsimile: 44-1707-373254

GREECE
N. ASTERIADIS S. A.
56-58, S. Trikoupi Str. P.O.Box 26140
GR-10022 Athens, Greece
Telephone: 30-1-823-5383
Facsimile: 30-1-823-9567

INDIA
Blue Star LTD. (HQ)
Analytical Instruments Department,
'Sahas'414/2 Veer Savarkar Marg,
Prabhadery Mumbai 400 025, India
Telephone: 91-22-5666-4068
Facsimile: 91-22-5666-4001

Blue Star LTD. (New Delhi)
Analytical Instruments Department,
E-44/12 Okhla Industrial Area,
Phase-11, New Delhi 110 020, India
Telephone: 91-11-5149-4000
Facsimile: 91-11-5149-4004

Blue Star LTD. (Calcutta)
Analytical Instruments Department,
7, Hare Street Calcutta 700 001, India
Telephone: 91-33-2248-0131
Facsimile: 91-33-2248-1599

Blue Star LTD. (Chennai)
Analytical Instruments Department, Lakshmi
Neela Rite Choice Chambers, 5, Bazullah Road,
3rd Floor T. Nagar Chennai 600 017, India
Telephone: 91-44-2815-8846
Facsimile: 91-44-2815-8015

INDONESIA
PT. TEKNOLABindo PENTA PERKASA
J1. Gading BukitRaya,
Komplek Gading Bukit Indah Blok I/11,
Kelapa Gading Jakarta 14240, Indonesia
Telephone: 62-21-45847057/58/59
Facsimile: 62-21)-45842729

IRAN
IMACO LTD.
No. 141 Felestin Ave.,
P. O. Box 13145-537, Tehran, Iran
Telephone: 98-21-6402191/6404148
Facsimile: 98-21-8978164

ITALY
JEOL (ITALIA) S.p.A.
Centro Direzionale Green Office Via Dei Tulipani,
1, 20090 Pieve, Emanuele (MI), Italy
Telephone: 39-2-9041431
Facsimile: 39-2-90414353

KOREA
JEOL KOREA LTD.
Sunmin Bldg. 6th F1.,218-16, Nonhyun-Dong,
Kangnam-Ku, Seoul, 135-010, Korea
Telephone: 82-2-511-5501
Facsimile: 82-2-511-2635

KUWAIT
YUSUF I. AL-GHANIM & CO. (YIACO)
P. O. Box 435, 13005 - Safat, Kuwait
Telephone: 965-4832600/4814358
Facsimile: 965-4844954/4833612

MALAYSIA
JEOL (MALAYSIA) SDN. BHD. (359011-M)
205, Block A, Mezzanine Floor,
Kelana Business Center97,
Jalan SS 7/2, Kelana Jaya,
47301 Petaling Jaya, Selangor, Malaysia
Telephone: 60-3-7492-7722
Facsimile: 60-3-7492-7723

MEXICO
JEOL DE MEXICO S.A. DE C.V.
Av. Amsterdam #46 DEPS. 402
Col. Hipodromo, 06100 Mexico D. F. Mexico
Telephone: 52-5-55-211-4511
Facsimile: 52-5-55-211-0720

PAKISTAN
Analytical Measuring System (Pvt.) Limited. AMS House
Plot # 14C, Main Sehar Commercial Avenue,
Commercial Lane 4,
Khayaban-e-Sehar,
D.H.A Phase 7, Karachi, Pakistan
Telephone: 92-21-5345581/5340747
Facsimile: 92-21-5345582

PANAMA
PROMED S.A.
Parque Industrial Costa del Este
Urbanizacion Costa del Este
Apartado 6281, Panama, Panama
Telephone: 507-269-0044
Facsimile: 507-263-5622

PHILIPPINES
PHILAB INDUSTRIES INC.
7487 Bagtikan Street, SAV Makati, 1203 Metro,
Manila Philippines
Telephone: 63-2-896-7218
Facsimile: 63-2-897-7732

PORTUGAL
Izasa. Portugal Lda.
R. do Proletariado 1,
2790-138 CARNAXIDE Portugal
Telephone: 351-21-424-7300
Facsimile: 351-21-418-6020

SAUDI ARABIA
ABDULREHMAN ALGOSAIBI G. T.B.
Algosaibi Bldg., Airport Rd., P. O. Box 215,
Riyadh 11411, Saudi Arabia
Telephone: 966-1-479-3000
Facsimile: 966-1-477-1374

SCANDINAVIA
JEOL (SKANDINAVISKA) A.B.
Hammarbacken 6 A, Box 716
191 27 Sollentuna, Sweden
Telephone: 46-8-28-2800
Facsimile: 46-8-29-1647

SERVICE & INFORMATION OFFICE
JEOL NORWAY
Ole Deviks vei 28, N-0614 Oslo, Norway
Telephone: 47-2-2-64-7930
Facsimile: 47-2-2-65-0619

JEOL FINLAND
Ylakaupinkuja 2, FIN-02360 Espoo, Finland
Telephone: 358-9-8129-0350
Facsimile: 358-9-8129-0351

JEOL DENMARK
Naverland 2, DK-2600 Glostrup, Denmak
Telephone: 45-4345-3434
Facsimile: 45-4345-3433

SINGAPORE
JEOL ASIA PTE. LTD.
29 International Business Park,
#04-02A Acer Building,
Tower B Singapore 609923
Telephone: 65-6565-9989
Facsimile: 65-6565-7552

SOUTH AFRICA
ADI Scientific (Pty) Ltd.
109 Blandford Road, North Riding,Randburg
(PO box 71295 Bryanston 2021)
Republic of South Africa
Telephone: 27-11-462-1363
Facsimile: 27-11-462-1466

SPAIN
IZASA. S.A.
Aragoneses, 13,
28100 Alcobendas,
(Polígono Industrial) Madrid, Spain
Telephone: 34-91-663-0500
Facsimile: 34-91-663-0545

SWITZERLAND
JEOL(GERMANY)GmbH
Oskar-Von-Miller Strasse 1,
85386 Eching Germany
Telephone: 49-8165-77346
Facsimile: 49-8165-77512

TAIWAN
JIE DONG CO., LTD.
7F, 112, Chung Hsiao East Road, Section 1, Taipei,
Taiwan 10023, Republic of China
Telephone: 886-2-2395-2978
Facsimile: 886-2-2322-4655

JEOL TAIWAN SEMICONDUCTORS LTD.
11F, No. 346, Pei-Ta Road, Hsin-Chu City 300,
Taiwan Republic of China
Telephone: 886-3-523-8490
Facsimile: 886-2-523-8503

THAILAND
BECTHAI BANGKOK EQUIPMENT
& CHEMICAL CO., Ltd.
300 Phaholyothin Rd. Phayathai,
Bangkok 10400, Thailand
Telephone: 66-2-615-2929
Facsimile: 66-2-615-2350/2351

THE NETHERLANDS
JEOL (EUROPE) B.V.
Tupolevlaan 28-A, 1119 NZ Schiphol-Rijk,
The Netherlands
Telephone: 31-20-6533088
Facsimile: 31-20-6531328

TURKEY
TEKSER LTD. STI.
Acibadem Cad. Erdem Sok. Baver Art. 6/1
34660 Uskudar/Istanbul-Turkey
Telephone: 90-216-3274041
Facsimile: 90-216-3274046

UAE
BUSINESS COMMUNICATIONS LLC.
P. O. Box 2534, Abu Dhabi UAE
Telephone: 971-2-6348495
Facsimile: 971-2-6316465

USA
JEOL USA, INC.
11 Dearborn Road, Peabody, MA. 01960, U. S. A.
Telephone: 1-978-535-5900
Facsimile: 1-978-536-2205/2206

JEO USA, INC. WEST OFFICE
5653 Stoneridge Drive Suite
#110 Pleasanton, CA. 94588 U. S. A.
Tel: 1-925-737-1740
Fax: 1-925-737-1749

VENEZUELA
MITSUBISHI VENEZOLANA C. A.
Avenida Francisco de Mirande Los Palos Grandes,
Carecas, Venezuela
Telephone: 58-212-209-7402
Facsimile: 58-212-209-7496

(Ser. No. 122)

No. 0901K431C Printed in Japan, Kp